Composites Part B 284 (2024) 111685

Contents lists available at ScienceDirect

Composites Part B

journal homepage: www.elsevier.com/locate/compositesb

Flexibility, toughness, and load bearing of 3D-printed chiral kerf composite structures

Aryabhat Darnal [a], Kanak Mantri [a], Will Betts [a], Negar Kalantar [b], Jeeeun Kim [c], Anastasia Muliana [a,*]

[a] Department of Mechanical Engineering, Texas A&M University, USA
[b] California College of the Arts, USA
[c] Department of Computer Science, Texas A&M University, USA

ARTICLE INFO

Handling Editor: Dr Uday Vaidya

Keywords:
Kerfing
Chiral and fractal structures
3D printing polymer
Nonlinear mechanical performance
Programmable composite materials

ABSTRACT

Chiral kerf structures are formed by arranging chiral and coiled unit cells which allows for multi-dimensional and multi-scale shape configurations under mechanical loadings. In this study, we investigate how the mechanical properties of materials and microstructural topologies interact to control the flexibility, toughness, and load bearing of 3D-printed chiral kerf structures. We explore chiral kerf structures with two different kerf patterns, i.e., square and hexagon, and three coiling densities. We consider three materials, namely brittle Polylactic Acid (PLA), compliant thermoplastic polyurethane (TPU), and a ductile composite made by alternating PLA and TPU, referred to as a programmable composite. The chiral kerf structures undergo two deformation mechanisms when subjected to mechanical loadings. The first one results from reconfigurations of kerf cells such as uncoiling, rotation of cells, and cell packing, and the second mechanism arises from nonlinear and inelastic material responses. The use of brittle material limits cell reconfigurations before material failure, reducing the overall flexibility and toughness of kerf structures. While the compliant material enables full cell reconfigurations, it results in low load bearing. The use of PLA:TPU composite allows for cell reconfigurations and inelastic material response, enhancing flexibility and toughness while maintaining a relatively high load bearing. We demonstrate that stress distribution in kerf structures can be controlled by using multiple materials or coil densities. This strategy can delay failure and improve the toughness and load-bearing capabilities of kerf structures.

1. Introduction

Advances in computer-aided design and computer graphics have facilitated freedom in structural design towards complex geometries, referred to as freeform structures. Freeform structures are not merely intended for their aesthetic appeal, but they can offer substantial functionality. A classic example is a dome that displays an elegant shape while demonstrating higher stiffness and load bearing than a flat plate. Freeform structures can be designed to promote shape reconfigurations upon external stimulation, further enhancing their functionality. Given their aesthetic and functional features, freeform structures find potential uses in various engineering applications in architecture, aerospace, civil, mechanical, and biomedical engineering [1–4] as well as in arts and crafts. For example, reconfigurable freeform structures are suitable for deployable antennas and stents [5–10], adaptive thermal insulation, shading facades [11,12], and morphing aircraft [13–15]. Reconfigurable freeform structures can potentially be used in robotics and stretchable electronics as well as for controlling wave propagation under dynamic loadings.

One particular interest is in creating reconfigurable freeform structures out of planar surfaces. Origami and kirigami approaches (Fig. 1a and **b**) have been used to create complex geometries through the folding and/or cutting of planes [16]. For example, Zirbel et al. [17] developed origami-based deployable foldable rigid panels with finite thickness to maximize the ratio of deployed to stowed dimension. The main challenge in the origami structure resided in the fabrication process to create crease lines out of structural materials with a finite thickness [18–20]. Li et al. [21] used the kirigami approach to fabricate reconfigurable metamaterials with multiple shape transformations. Since the kirigami approach relies on structural instability mechanisms to attain shape reconfigurations, they are typically in the form of slender structures to easily trigger instability [22]. Lattice and chiral structures (Fig. 1c) have

* Corresponding author.
E-mail address: amuliana@tamu.edu (A. Muliana).

https://doi.org/10.1016/j.compositesb.2024.111685
Received 15 April 2024; Received in revised form 27 June 2024; Accepted 30 June 2024
Available online 4 July 2024
1359-8368/© 2024 Elsevier Ltd. All rights are reserved, including those for text and data mining, AI training, and similar technologies.

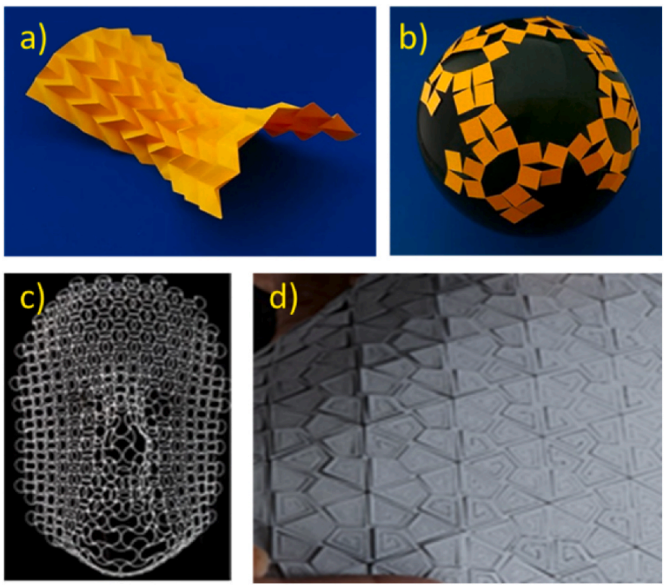

Fig. 1. Freeform structures out of origami and kirigami structures (a and b [16], [11]), lattice structure (c [33], [22] and kerf structure (d).

been used to create reconfigurable freeform structures [23–26]. Typical lattice reconfigurable structures are formed by arrangements of closed cells, whose reconfigurability is dominated by in-plane cell deformations.

Another approach to generating complex 3D shapes out of rigid planar surfaces that enable the creation of freeform structures is by relief cutting or *kerfing*. Kerfing is a subtractive manufacturing process that involves removing material from relatively stiff planar structures out of engineered woods [27,28], polymer [29], metals, and alloys (Fig. 1d). Within kerf structures, various cut patterns can be designed not only to induce panel flexibility but also to incorporate other functionalities. For example, kerf patterns could control dynamics responses and wave propagations [11,12] and tuned room acoustic characteristics [30–32]. The multi-dimensional and multi-scale flexibility of kerf structures allows for in-plane and out-of-plane shape reconfigurations at different length scales, which potentially be used for adaptive structures without compensating their load bearing.

Recent studies have adopted the traditional square Archimedean kerf patterns and used 3D printing polymers to study their deformations. Kerf patterns belong to a class of chiral and fractal structures owing to their repeated orders of microstructures and asymmetric cell arrangements. Chiral patterns allowed for cell reconfigurations when subjected to mechanical loading [34]. The arrangement of the elements in the chiral pattern enabled coupling deformations such as converting uniaxial force into a twisting motion [35,36]. Zhang et al. [37] investigated the bending behavior of kerf structures with a square Archimedean pattern out of polymer. Through three-point bending tests and finite element analysis, they showed that the introduction of kerf fractal cuts altered the energy dissipation, shape recoverability, and compliance. Increasing the order of kerf fractal cuts decreased the bending stiffness while sharply improving the recoverability when the load is removed. Wang et al. [38] 3D printed kerf fractal structures out of polymers with the stretchability of up to 360 % strain for applications in soft electronics and soft robotics. The high stretchability was attributed to the multiple-order uncoiling of the square Archimedean kerf pattern.

Many efforts in investigating chiral, fractal, and kerf structures have centered on finding proper geometrical patterns to tune structural functionalities such as increasing flexibility and energy dissipation. The materials used in the chiral, fractal, and kerf structures play crucial roles in shape reconfigurations and functional performances of the structures. A recent study by Darnal et al. [28] highlighted how the viscoelastic deformations of wood and plastic deformations of stainless-steel kerf structures affected shape reconfigurations. In this study, we investigate the interplay of different mechanical behaviors of materials and microstructural topologies in controlling the flexibility, toughness, and load bearing of 3D-printed chiral kerf structures. We consider three different materials, i.e., Polylactic Acid (PLA), Thermoplastic Polyurethane (TPU), and a programmable composite with a 50PLA:50TPU volume ratio. These materials have significantly different mechanical properties. PLA is brittle with relatively high load bearing and stiffness while TPU is stretchable with significantly low load carrying ability. Recent efforts on developing programmable filaments [27] suitable for low-cost FDM printing have shown the ability to tune the mechanical properties of printed objects out of PLA:TPU programmable filaments that enabled achieving new mechanical performance, i.e., high strength, stiffness, and toughness and increased damping ability [39–41]. As for the kerf pattern, we study kerf cells of square and hexagon chiral patterns with three different coil (spiral) densities. Although varying cell sizes alter cell flexibility, in this study we consider a constant cell size. The organization of this paper is as follows. **Section 2** presents kerf patterns and material properties. **Section 3** discusses testing kerf unit cells and modeling the mechanical performance of kerf unit cells. **Section 4** presents analyses of kerf panels under uniaxial tension and bending. **Section 5** presents conclusions from this study and future explorations.

2. Kerf patterns and materials used for chiral kerf structures

2.1. The effect of cell geometrical parameters on cell deformability

We consider two kerf patterns, namely square interlocked Archimedean spiral [42] and hexagon spiral [43], as building blocks, see Fig. 2. These patterns are relatively easy to arrange to form large-scale structures. A detailed discussion of various kerf topologies and their corresponding deformability can be found in Refs. [44–46]. Most previous studies focused on the use of wood-based materials. Kerf cells with different coil (revolving spiral or cutline) densities in both patterns, namely low density (LD), medium density (MD), and high density (HD) are examined. The LD cell has the smallest number of coiling to create a kerf cell within the specific pattern, while the MD and HD increase the number of coiling by a factor of 1. The number of coiling can be referred to as fractal order. The studied cells with square and hexagon patterns have a side length of 1 in. and a thickness of 0.125 in. The kerf cells are formed by arrangements of straight prismatic bars with a rectangular cross-section of dimension t x w. The slenderness ratios of the prismatic bars, measured by the ratio of the length to the cross-section dimensions of the bar, in the cells govern the flexibility of the cells, hence the flexibility of the overall kerf structures.

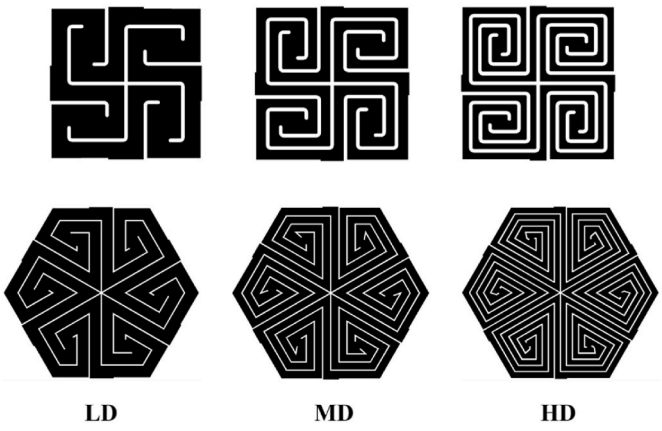

Fig. 2. Square Archimedean (top) and hexagon (bottom) kerf patterns.

The studied square kerf cells are stiffer compared to the hexagon kerf cells. This is because each bar segment in the square kerf cells has a smaller slenderness ratio compared to those of the hexagon kerf cells for the same fractal order. Table 1 summarizes the geometrical parameters of kerf cells and Table 2 lists the total length of the beam segments in each kerf cell. A higher total length of the kerf cells can increase toughness and extensibility attributed to the uncoiling of the cells, which we will discuss later. To examine the influence of geometrical parameters of the load transfer in kerf cells under uniaxial tension, we determine a geometric tortuosity, r_G, which is defined by the ratio of the total length of the beam segment to the shortest length for load transfer in the kerf cell (see Table 3). The shortest length of the square cell is 1″ and for the hexagon cell is 1.65". A higher value of r_G leads to higher flexibility (lower stiffness) and a longer path of load transfer along the beam segments in the kerf cells, which is attributed to the ability of the kerf cell to uncoil.

2.2. The effect of elastic moduli of materials on cell deformability

The materials used for fabricating the kerf cells are PLA, TPU, and programmable polymer out of PLA:TPU with a volume ratio of 50:50. Detailed information on the materials is given in Appendix A. The elastic moduli of the PLA, TPU, and 50PLA:50TPU printed polymers are 522, 1.85, and 261 ksi, respectively. Fig. 3 shows the 3D-printed square and hexagon kerf cells for all three coil densities.

We examine the interplay of the cell geometrical parameters (Table 1) and elastic modulus of the cell material on the bending flexibility parameter of the kerf cells, as illustrated in Fig. 4. The bending flexibility of the beam segments is represented by the ratios of L^3/EI_{yy} and L^3/EI_{zz} where L, I_{yy} and I_{zz} are the length of the longest beam segment in the kerf cell, second moment of area about the y and z axes, respectively. The kinematic representation of the beam segment of the kerf unit cells is shown in Figure A2 of Appendix A. The in-plane bending of the beam segments of kerf cells is controlled by the value of L/w and L^3/EI_{zz}, while the out-of-plane bending is by the value of L/t and L^3/EI_{yy}.

Table 1
Geometrical properties of the beam segment in kerf cells (size of cells is 1 inch).

Kerf Pattern	Coil Density	Area (in^2) t x w	The second moment of the area		Slenderness ratio	
			I_{zz} ($\times 10^{-5}$ in^4)	I_{yy} ($\times 10^{-5}$ in^4)	L/w[a]	L/t[a]
Square	LD	0.125 × 0.10	1.042	1.628	4.8	3.84
	MD	0.125 × 0.06	0.225	0.976	8	3.84
	HD	0.125 × 0.04	0.067	0.651	12	3.84
Hexagon	LD	0.125 × 0.10	1.042	1.628	8.5	6.8
	MD	0.125 × 0.07	0.357	1.139	12.1	6.8
	HD	0.125 × 0.05	0.130	0.814	17	6.8

[a] From the longest beam segment.

[1] Reprinted with permission from "From flat sheets to curved geometries: Origami and kirigami approaches" by Callens, S. J., & Zadpoor, A. A., (2018). Materials Today, 21(3), 241–264, Copyright [2018] by Elsevier.

[2] Reprinted with permission from "Shape-shifting structured lattices via multimaterial 4D printing" by Boley, J.W., Van Rees, W.M., Lissandrello, C., Horenstein, M.N., Truby, R.L., Kotikian, A., Lewis, J.A. & Mahadevan, L., (2019). Proceedings of the National Academy of Sciences, 116(42), 20856–20862., Copyright [2019] by PNAS.

Table 2
Total length of the beam segments in square and hexagon kerf cells.

Geometry	LD	MD	HD
Square	6.92″	11.29″	15.23″
Hexagon	20.14″	30.71″	40.61″

Table 3
Geometric tortuosity for square and hexagon kerf cells.

Geometry	r_G		
	LD	MD	HD
Square	6.92	11.29	15.23
Hexagon	12.21	18.61	24.61

The TPU kerf cells are the most flexible owing to the higher value of L^3/EI_{zz} and L^3/EI_{yy}. The above kerf cells are easier to deform out-of-plane than in-plane. Within a linear behavior, the deformation of kerf cells is inversely proportional to their modulus and second moments of area of beam segments.

3. Testing and modeling of kerf unit cells under uniaxial tension

3.1. Experimental testing of kerf unit cells

We performed a uniaxial tensile test until failure to the kerf cells in an Instron 5984 Floor Standing Universal Testing Machine with 5 kN load cell. One arm of the unit cell was fixed, and the opposite arm was stretched at a displacement rate of 0.04 in/s. To ensure the repeatability of these tests, we performed three repeated tests for each kerf cell. Fig. 5 summarizes the experimental results for the square and hexagon cells. The tensile responses correspond to the cell reconfiguration and mechanical behaviors of the materials, as depicted in Fig. 6. The brittle PLA limits cell uncoiling, and failure is dominated by PLA breakage. The compliant TPU undergoes full uncoiling without material failure. Using ductile composites facilitates simultaneous geometrical and material responses, i.e., cell uncoiling, out-of-plane rotation, and inelastic straining of the beam segments.

The correlation between deformed shapes and force-displacement responses is depicted in Fig. B1 of Appendix B. The different deformation mechanisms of kerf cells of various materials have pronounced impacts on the toughness, maximum load, final displacement, and initial stiffness of the kerf cells, summarized in Fig. 7. A table presenting the quantitative values is added in Table B1 in Appendix B. For the PLA and programmable composite kerf cells, the toughness was determined until the failure displacement, and for the TPU kerf cells, it was determined at the last recorded displacement value as TPU kerf cells did not fail during the testing. The square and hexagon kerf cells out of programmable composite show the highest toughness. The square LD kerf cells out of the PLA exhibit the highest stiffness and maximum load. The hexagon kerf cells with the compliant TPU and ductile programmable composite demonstrate the highest cell extensibility (final displacement). The hexagon cells generally have higher toughness and final displacement than the square kerf cells. The square cells have a higher maximum load and stiffness for a brittle PLA than the hexagon cells.

The combination of cell uncoiling and inelastic straining along the beam segments can significantly enhance the toughness, maximum load, and final displacement of kerf cells as observed in the hexagon kerf cell with the programmable composite (see Fig. 8).

3.2. Modeling kerf cells

We present finite element (FE) analyses of kerf cells to gain insight into the mechanisms governing the geometrical and material responses of kerf cells under uniaxial tension. Each segment in the kerf cells is

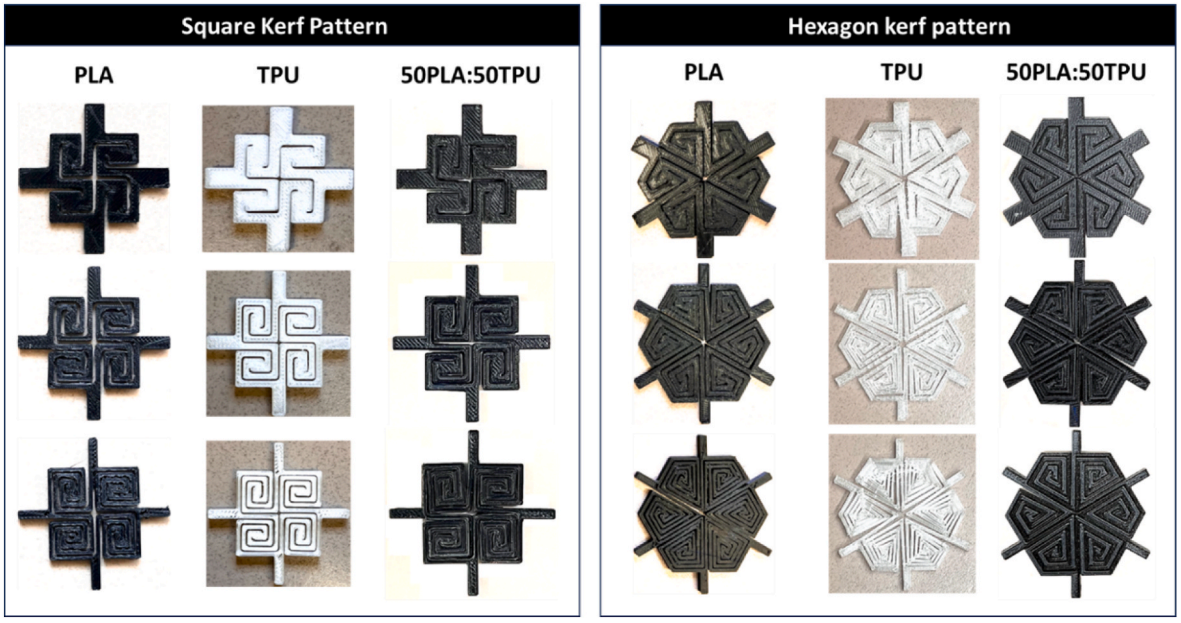

Fig. 3. Kerf cells with PLA, TPU, and PLA:TPU composite and different coiling densities (from top to bottom: LD, MD, and HD).

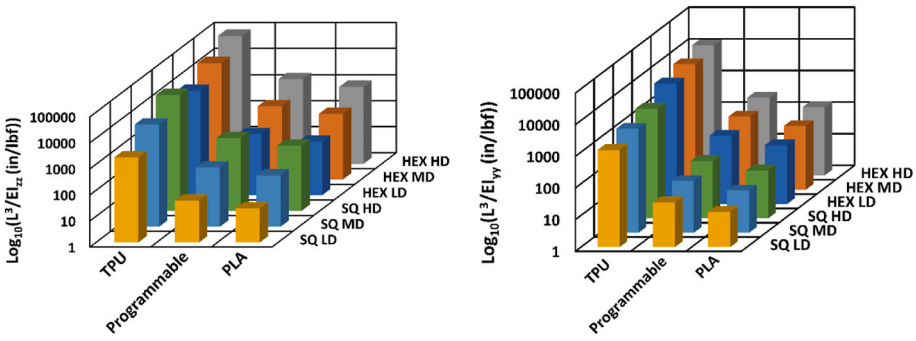

Fig. 4. Variation of elastic bending flexibility parameter of kerf cells with material and geometry.

modeled using a nonlinear beam element (B31) in ABAQUS CAE analysis. The B31 beam element in ABAQUS incorporates axial stretching, transverse shearing, bending, and twisting of a noncircular cross-section where warping can occur. A more detailed discussion of the FE analyses of kerf cells is given in Appendix C.

Fig. 9 compares tensile behaviors between the experimental and simulation results of kerf cells with the square and hexagon patterns. For the PLA kerf cells, the responses are fairly linear before failure and the beam element model with the material softening strategy captures the brittle failure. Figures C2 and **C.3** in Appendix C depict the corresponding deformed shapes, from the experiment and simulation, of the PLA kerf cells with square and hexagon patterns, respectively. Higher coiling densities result in larger deformations before failure attributed to the lower stresses of the beam segments and partial uncoiling before the breaking of the segments when the stress exceeds the tensile strength of the PLA. The hexagon kerf cells fail in stages from the consecutive breaking of the stressed vertexes.

For the TPU kerf cells, the beam model with the Yeoh hyperelastic material captures the uniaxial tensile deformation. For the LD cells, at higher displacement magnitudes, noise is seen in the experimental data due to the friction between the segments of the kerf cell. This is not captured by the beam model. For the LD kerf cells, the overall deformation before uncoiling is dominated by the elastic deformation of the TPU polymer. The uncoiling process causes fluctuation in the forces. Figures C4 and **C.5** show the deformed shapes of the TPU kerf cells. Figure C6 depicts microstructural changes in TPU LD kerf cells during loading and unloading, indicating that the kerf cells return to their initial configuration.

For the kerf cells with 50PLA:50TPU programmable composite, the heterogeneous nature of the programmable composite leads to a complex failure mechanism attributed to cell uncoiling, cascading material failure, and out-of-plane cell rotations. In the FE analyses, the programmable composite is treated as a homogeneous material with elastic-plastic deformation. The homogenized material model captures the overall force-displacement behaviors, as depicted in Fig. 9, but was limited in capturing the cascading material failure and cell rotations during the uncoiling stage. Figures C7 and **C.8** show the deformed shapes of kerf cells with the programmable composite.

3.3. Discussion on the tensile response of kerf cells

The deformations of the kerf cells with a relatively stiff material like PLA or a compliant material like TPU are governed mostly by the geometrical parameters (kerf patterns and coil densities) of kerf cells. In the case of PLA kerf cells, the beam segments exhibit a linear elastic response until the fracture initiates, which occurs at a later stage of deformations. In the case of TPU kerf cells, the low elastic modulus of TPU facilitates easy cell reconfiguration within a linear elastic material region that allows for the cells to fully uncoil. In our study, the testing fixture reached the maximum spans before we could push the TPU to

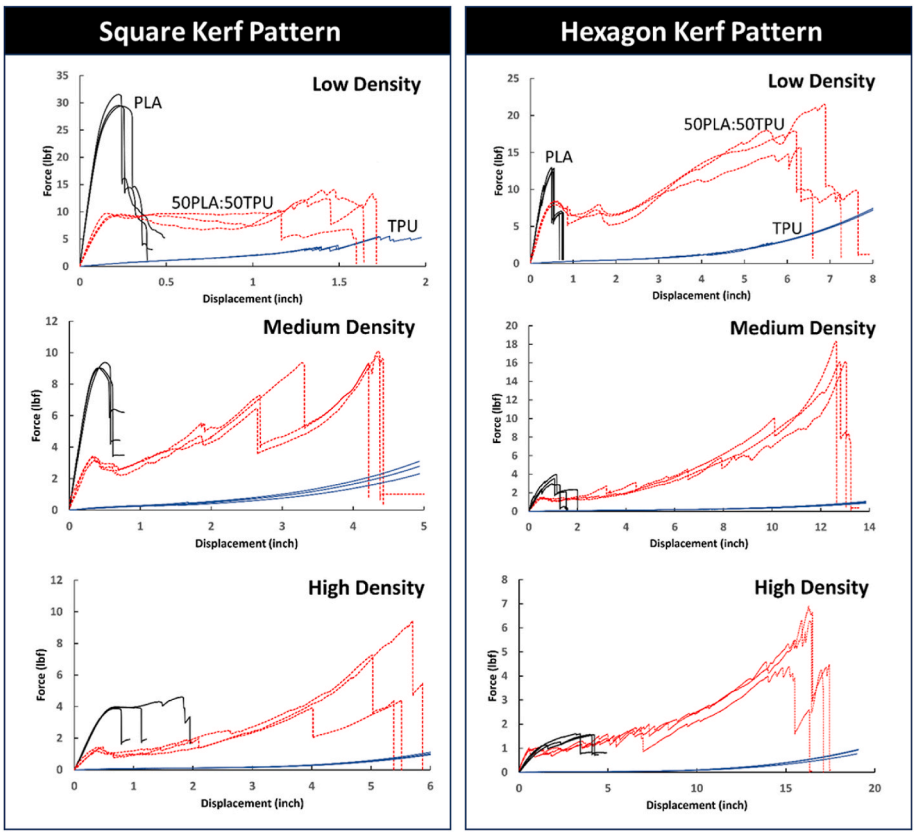

Fig. 5. Force-displacement curves for square and hexagon kerf cells of different coil densities and materials.

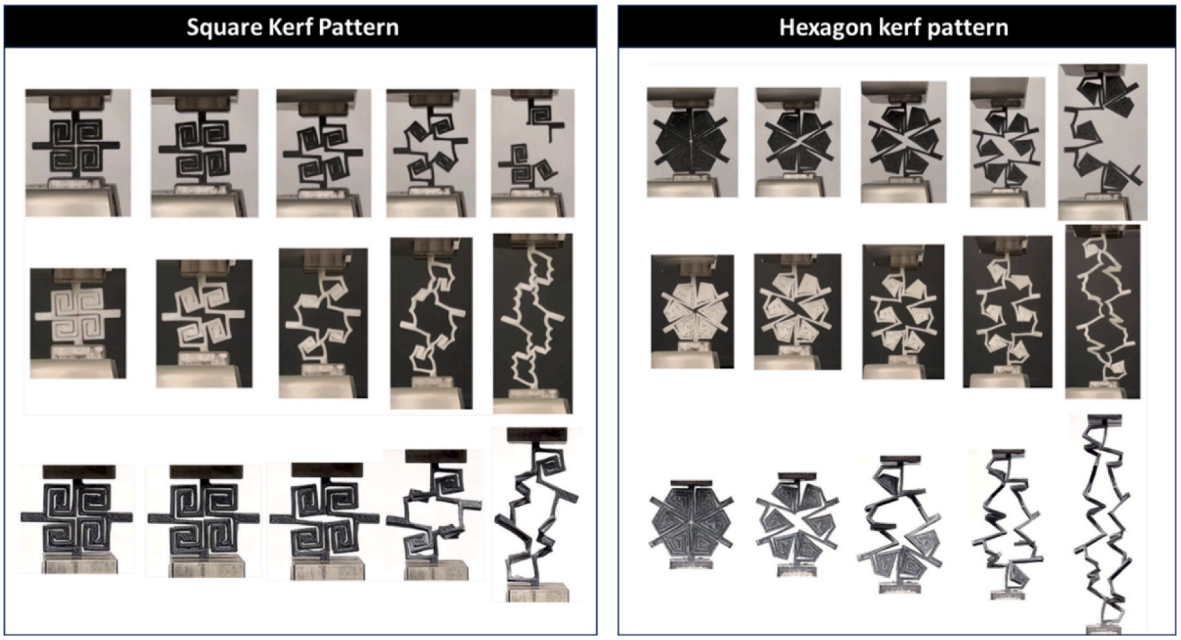

Fig. 6. Microstructural changes in square and hexagon kerf cells with MD cut out of PLA (top), TPU (middle), and 50PLA:50TPU (bottom).

exhibit nonlinear deformations and failure.

In the kerf cells with ductile programmable composite, the deformations are due to simultaneous geometrical and inelastic material responses. The initial deformation is governed by the elastic responses of the composite to promote cell uncoiling. Further straining causes more cells to uncoil and inelastic deformation of the programmable composite. The heterogeneous composite leads to cascading material failure, i.e., sequential load transfer from brittle PLA breakage to compliant TPU, altering the cross-sectional geometries of the beam segments. The changes in the cross-sectional geometries result in out-of-plane cell rotations.

The initial stiffness of kerf cells is influenced by their geometrical

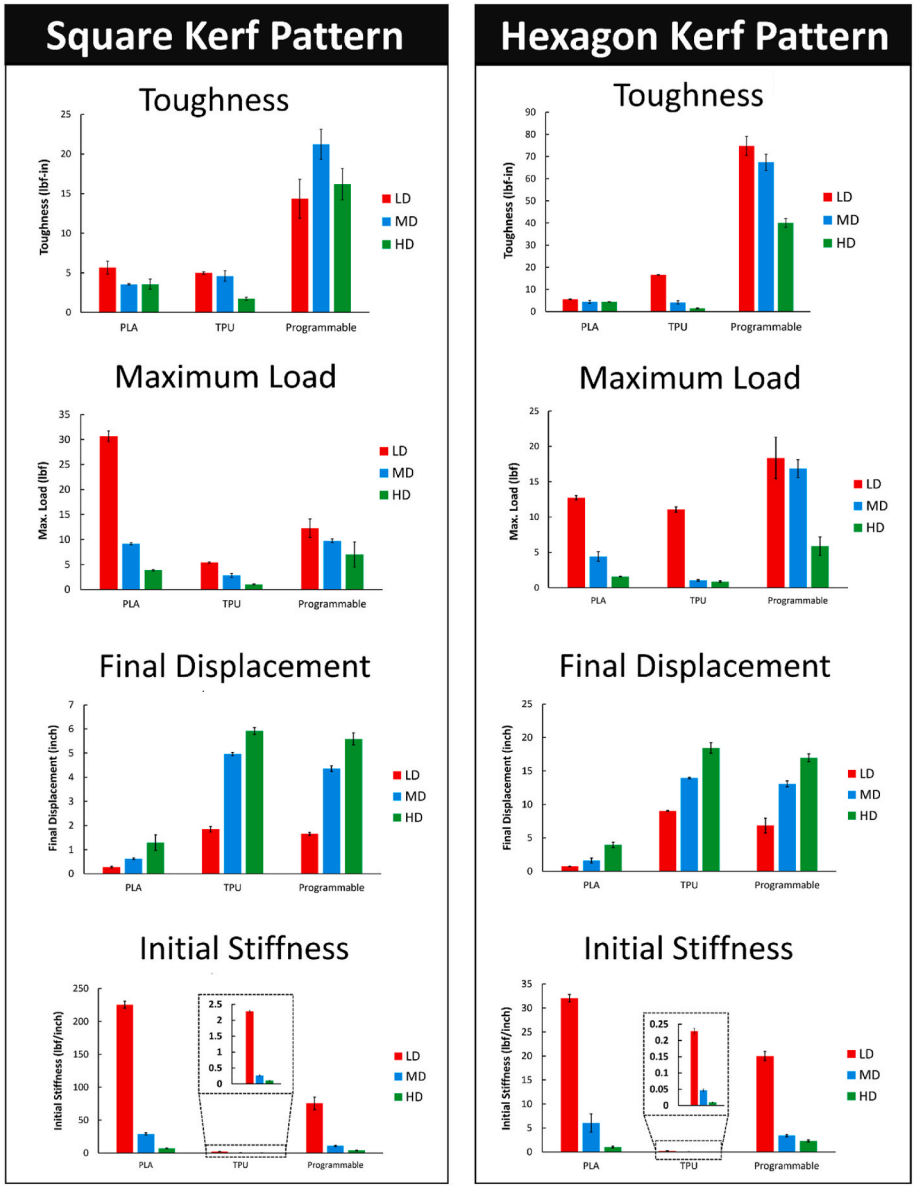

Fig. 7. Mechanical properties of kerf cells for square (left) and hexagon (right) patterns. Top to bottom properties are: toughness, maximum load, failure displacement, and initial stiffness.

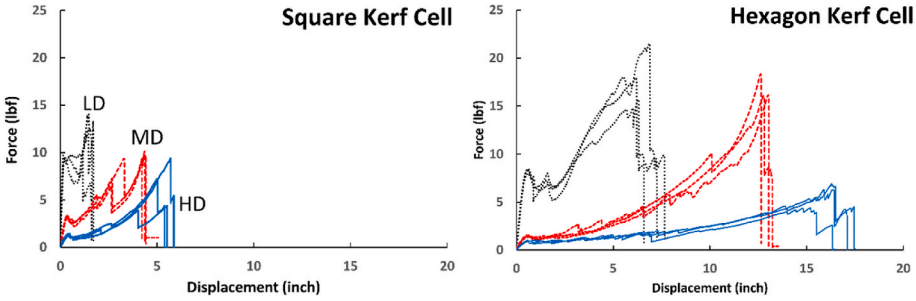

Fig. 8. Force-displacement curves for kerf cells with 50PLA:50TPU programmable composite.

parameters (Tables 1–3) and the elastic modulus of the material. The final displacement is governed by the ability of cells to uncoil and the failure strength of the materials. The elastic modulus and failure strength of the material and cell uncoiling ability control the toughness. The maximum load depends on the stress distribution in the cells. Cell reconfigurations such as uncoiling can lead to stress redistribution, delaying failure and enhancing maximum load.

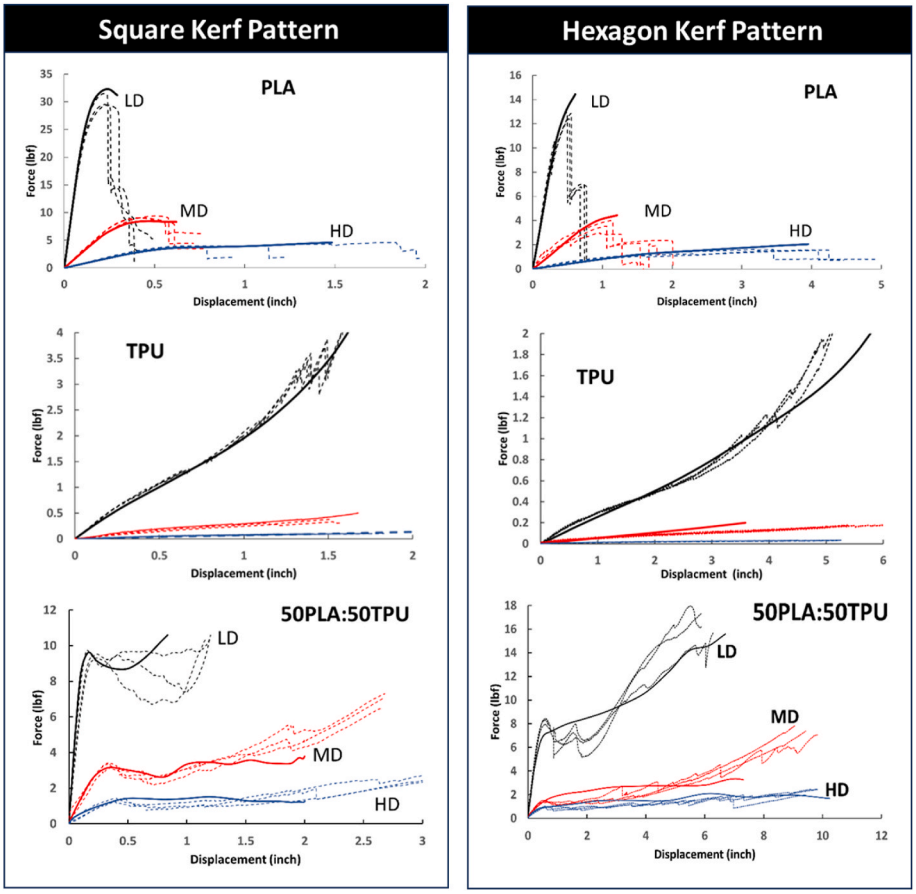

Fig. 9. Model and experiment comparisons for square and hexagon kerf cells (solid line refers to model and dashed line refers to experiment).

4. Analyses of kerf structures

We study the deformations of the planar kerf structures under uniaxial tension and bending. We explore the deformation mechanisms and their effects on the flexibility, toughness, and load bearing of kerf structures by varying kerf topologies and materials.

4.1. Uniaxial tension of kerf structures

We simulate planar kerf structures with square and hexagon kerf patterns under uniaxial tension. The square kerf structures have a dimension of 2 in x 5 in x 0.125 in and the hexagon kerf structures are 5 in x 8.6 in x 0.125 in (see Fig. 10). The design explorations of kerf structures are based on the following kerf topologies.

1) uniform coil density and uniform material.
2) uniform material with varying coil densities, i.e., HD cut for regions of highest flexibility and MD or LD cut for regions of lower flexibility, as discussed in Ref. [42].
3) uniform coil density, e.g., MD, and varying materials, i.e., TPU for regions of higher flexibility and programmable composite for other regions.

Fig. 11 presents the simulation results from the uniaxial tension of kerf structures. A displacement control was applied until material failure occurs, i.e., fracture of PLA and ductile failure of the programmable composite. In the kerf structures of uniform coil density and uniform material, at early loading (represented by a nearly linear force-displacement response) the tensile responses are mainly governed by cell rotations towards the loading axis with a linear elastic material response. Increasing loading demonstrates the interplay of geometrical

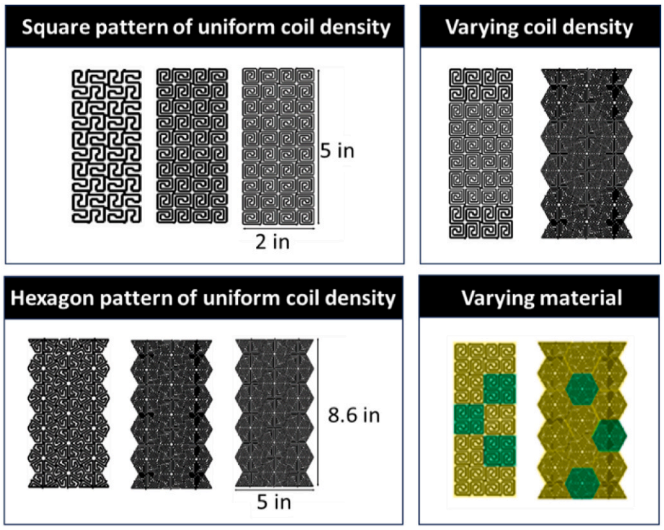

Fig. 10. Various designs of kerf structures with square and hexagon kerf patterns. For the varying materials, the green region indicates TPU and the yellow region indicates Programmable polymer. (For interpretation of the references to colour in this figure legend, the reader is referred to the Web version of this article.)

topology and nonlinear material responses. The nonlinear responses of materials, whether from brittle fracture in PLA, plastic deformation in programmable composite, or large stretch in TPU, alter cell reconfigurations and force-displacement paths (Fig. 11 a and b for the MD coil density).

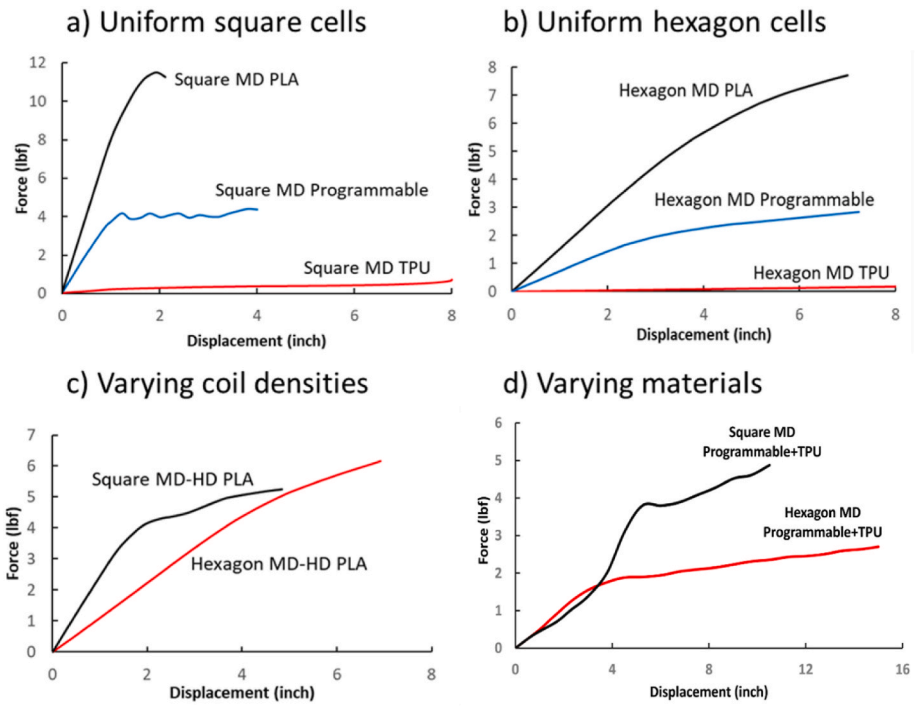

Fig. 11. Uniaxial tension force-displacement curves for kerf structures with: a) square pattern of MD coil density, b) hexagon pattern with MD coil density, c) varying coil densities of HD (central region) and MD (top and bottom regions), and d) varying TPU and programmable polymer.

For the kerf structure with square programmable composite, the waviness in the force-displacement response is due to the shear banding, indicated by nonuniform plastic deformations of the beam segments causing rotation and uncoiling of kerf cells that started from unconstraint regions of the kerf structure (Fig. 12a). The contour is shown for

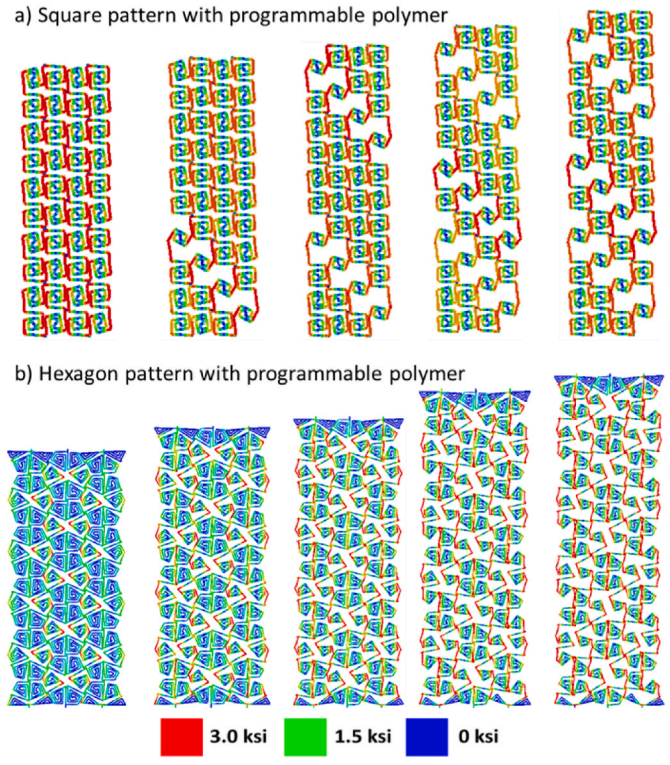

Fig. 12. Cell uncoiling of the square and hexagon programmable kerf structures under uniaxial tension.

von Mises stress and the yield limit for the programmable polymer is 3 ksi. The shear banding effect is not seen in the case of hexagon kerf topology with programmable composite. The hexagon kerf topology results in localized stresses on the vertices of kerf cells and uniform cell uncoiling (Fig. 12b). The same deformation mechanisms are shown for the kerf structures with LD and HD uniform coil densities (see Fig. D1).

In the kerf structures of varying coil densities in Fig. 10, the flexible cells (i.e., higher coil density) respond to the mechanical deformation at early loading (nearly a linear response depicted in Fig. 11c). At a later stage of loading, all cells deform, resulting in nonlinear responses. In the kerf structures of varying materials, adding compliant TPU locally within the programmable composite reduces stresses and alters stress patterns as illustrated in Fig. 13, which can be used to tune the overall responses i.e., stiffness, toughness, and load bearing, of kerf structures.

Fig. 14 summarizes the stiffness, toughness, and maximum load of kerf structures with square and hexagon patterns under uniaxial tension from the simulation. The square pattern results in higher stiffness under tension when compared to the hexagon pattern, while the hexagon pattern gives higher toughness. Like in the kerf cells discussed in **Section 3**, the stiffness is controlled by the geometrical properties (Table 1 and **3)** and the elastic modulus of the material. Microstructural changes from uncoiling cells contributed to increasing the toughness of the structures at moderate tensile deformations. The limited prescribed displacement prevents the complex failure mechanism of the programmable material from taking place, which could otherwise enhance the toughness and load bearing of the structures similar to the responses of the kerf cells.

To validate the simulation of the kerf structures under uniaxial tension, we performed experimental tests on selected 3D-printed kerf structures. We used a universal testing machine (Instron) with a 5 kN load cell using displacement control at a rate of 0.04 in/s. The lower handle of the kerf structure was fixed to the grip and the upper handle of the kerf structure was pulled uniaxially. Fig. 15 shows examples of 3D-printed planar kerf structures and experimental setups.

The force-displacement data from the experiment and simulation are compared, as shown in Figs. 16 and 17. A good correlation between the simulation and experimental data is observed, indicating that the beam

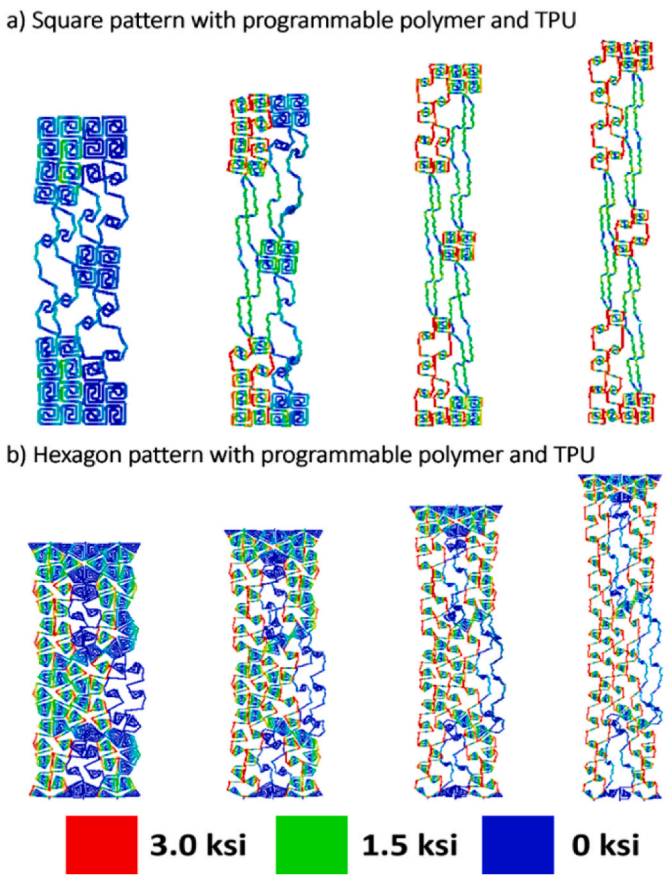

Fig. 13. Deformation behaviors of the kerf structures with programmable polymer and TPU.

element model is sufficient in describing the mechanical response of kerf structures with different kerf topologies and material behaviors. The deformation patterns of the kerf structures with square and hexagon kerf cells under the uniaxial tension are depicted in Figs. D2 and **D3**, respectively, of Appendix D. The deformed shapes of the kerf structures from the simulation and experiment agreed well. The deformed shapes confirm the shear band behaviors of the kerf structure with a square pattern out of programmable polymers (see Fig. D2c). The experiment indicates the out-of-plane cell rotations in addition to the cell uncoiling which is not captured by the simulation. The discrepancy is because the model assumes a homogeneous inelastic deformation for the programmable composite ignoring its heterogeneity nature.

4.2. Bending of kerf structures

For bending analyses, we consider kerf structures of dimension 5 in x 5 in x 0.125 in for the square pattern while for the hexagon pattern 8 in. x 8.6 in x 0.125 in. The information on the FE model is given in Appendix D. We examine several designs for kerf structures (see Fig. 18).

1) uniform coil density and uniform material.
2) uniform material with varying coil densities, i.e., HD for the region with higher curvature and MD with the region of lower curvature.
3) uniform density, i.e., MD, with varying materials, i.e., TPU for regions of higher curvature and PLA for regions of lower curvature.

The force-displacement responses of the uniform material and medium coil density with square and hexagon kerf patterns are illustrated in Fig. 19a and **b**, respectively. The hexagon kerf structures overall show more flexible deformations under bending as compared to the corresponding square kerf structures, owing to the geometrical parameters. Similar bending behaviors are observed for the kerf structures with square and hexagon patterns of different coil densities for PLA, TPU, and programmable composite, as shown in Fig. D5 in Appendix D.

When using a stiff PLA, cell packing leads to a stiffening of the kerf structure under bending. The hexagon cells result in uniform stress transfer along the cell sides that prevents stress concentration unlike in the square cells (see Fig. D6). Varying coil density in the kerf structures with stiff PLA improves the bending flexibility while maintaining the relatively high load bearing (Fig. 19c) and reduces localized stresses as depicted in Fig. D7. When using soft TPU the overall stiffening of the kerf structures is attributed to the hyperelastic deformations of the material. The high flexibility of the hexagon TPU kerf structure causes the waviness in the force-displacement curves from the local uncoiling of the cells, shown in Fig. D8. Varying the material in the kerf structures, i.e., using TPU within a stiff PLA, increases bending curvature. However, the deformation is mostly localized in the TPU regions. When using the programmable composite, we can see the interplay of inelastic material responses and cell packing of the kerf structures (Fig. D9), but the stiffening responses are not observed.

Fig. 20 summarizes the stiffness, toughness, and maximum load of kerf structures with square and hexagon patterns under bending. The square pattern results in higher stiffness of kerf structures when compared to the hexagon pattern, owing to the geometrical factor of kerf cells (Tables 1 and 3). For the toughness and maximum load, the square and hexagon patterns are comparable with slightly higher toughness in the hexagon pattern and slightly higher maximum load in the square pattern. Under bending, the microstructural configurations are due to cell packing. Better packing of cells of hexagon kerf structures improves load bearing. Varying coil density in a kerf structure with a stiff material is shown effective in maintaining good stiffness, toughness, and load bearing under bending, which was due to better control of stress distribution.

To validate the numerical results, we performed bending experiments on selected 3D-printed kerf structures, as illustrated in Fig. 21. We considered a 3-point bending test, following the specifications of ASTM D790–17 which recommends an overhang on each end of at least 10 % of the support span [47]. The three-point bending experiments were carried out using a universal testing machine (Instron) with a 5 kN load cell using displacement control at a rate of 0.0033 in/s. The experimental setup is illustrated in Fig. 22. The distance between the supporting pins was set such that they were equidistant from the center of the kerf structures. A cylindrical indenter, printed using PLA, was attached to the upper grip of the Instron Machine to displace the central region of the kerf panel. The diameter of the indenter was 0.6 in. The indenter was displaced by 0.75 in. to deform the kerf structure and the reaction force on the upper grip was recorded. Pushing the indenter larger than 0.75 in. resulted in significantly large rotation and slipping of the samples.

The simulation and experimental results show good agreement in the quantitative response and bending shapes (see Fig. 22). The limited testing setup precluded applying a much larger bending displacement to push the loading in the nonlinear regime as shown in the simulation.

4.3. Discussion on tensile and bending responses of kerf structures

In both brittle and compliant kerf structures under tensile loading, the deformations are mostly governed by cell uncoiling with a linear elastic material response, and only at a later stage of deformations, the material fracture or nonlinear deformations are observed. In kerf structures out of ductile programmable composite and square kerf cells, a continuous axial stress along the loading direction under uniaxial tension creates ductile shearing which gives rise to shear banding. The shear banding can be avoided by eliminating continuous axial stress, like in the hexagon kerf pattern, as depicted in Fig. 12.

In kerf structures out of materials with relatively high elastic modulus like in PLA and programmable composite, bending leads to cell

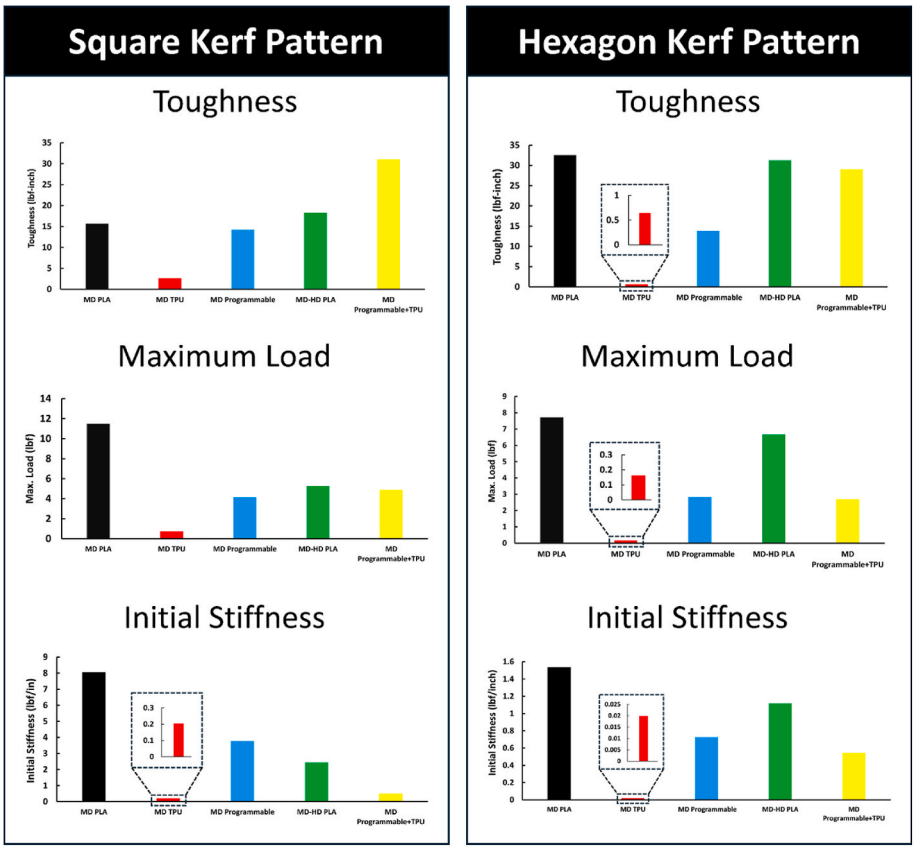

Fig. 14. Mechanical properties of kerf structures under tensile load for square and hexagon patterns. Top-to-bottom properties are initial stiffness, toughness, and maximum load.

Fig. 15. Experimental setup for square and hexagon kerf structures under uniaxial tension.

packing from high resistant contact stresses among neighboring cells. A similar response is seen in other studies out of PMMA and VeroWhite Resin [37,48,49]. A better packing deformation into curved surfaces is seen in the hexagon kerf topology (i.e., hexagons can better fit into a dome shape without overlaps or gaps). The hexagon cells lead to more uniform stress transfer along the cell sides that prevents stress concentration unlike in the square cells. When using brittle materials, cell packing leads to stiffening in the overall bending deformation due to increasing contact stresses with increasing bending curvatures. When using a ductile material like in the programmable composite, cell packing induces plastic deformation in the material, preventing stiffening behavior. In kerf structures out of a compliant material, cell uncoiling and stretching of the material dominate the bending responses.

The beam segments that link different kerf cells exhibit localized stresses, which can lead to segment failures. The localized stresses can be redistributed and minimized by varying coil density or material across the kerf structures. The idea is to enable easy cell reconfiguration with

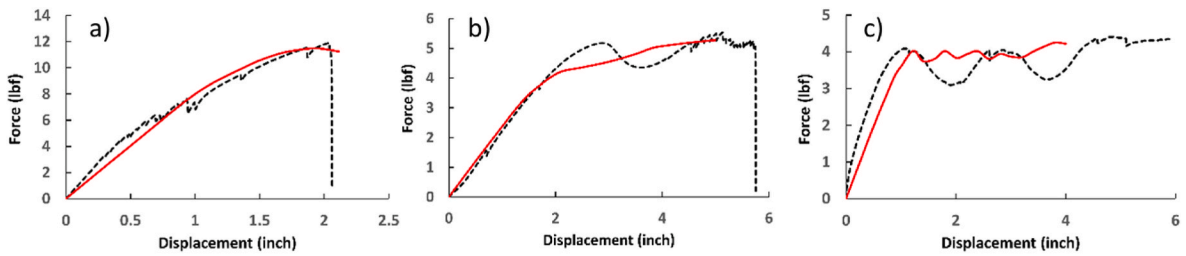

Fig. 16. Force-displacement responses of kerf structures with square kerf pattern under uniaxial tension. a) MD of PLA; b) MD-HD of PLA, c) MD programmable polymer. The red solid line represents the simulation and the black dashed line represents the experimental data. (For interpretation of the references to colour in this figure legend, the reader is referred to the Web version of this article.)

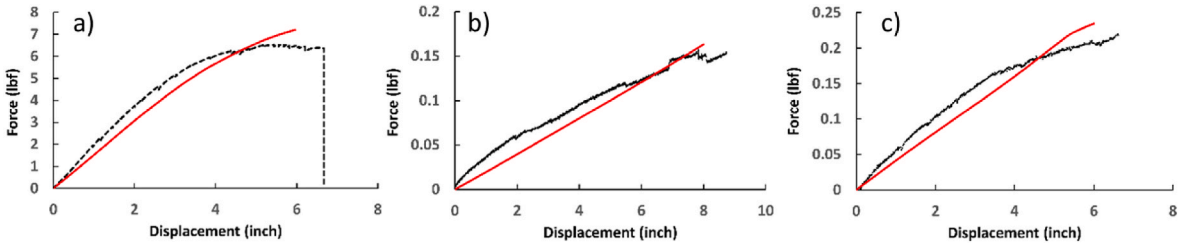

Fig. 17. Force-displacement responses of kerf structures with a hexagon pattern under uniaxial tension. a) MD PLA, b) MD TPU, and c) MD with varying PLA-TPU. The red dashed line represents the simulation and the solid black line represents the experimental data. (For interpretation of the references to colour in this figure legend, the reader is referred to the Web version of this article.)

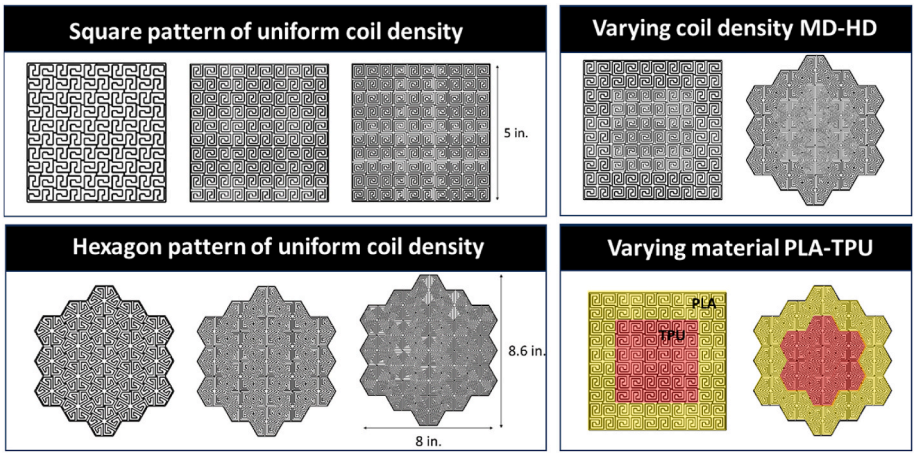

Fig. 18. Various designs of kerf structures.

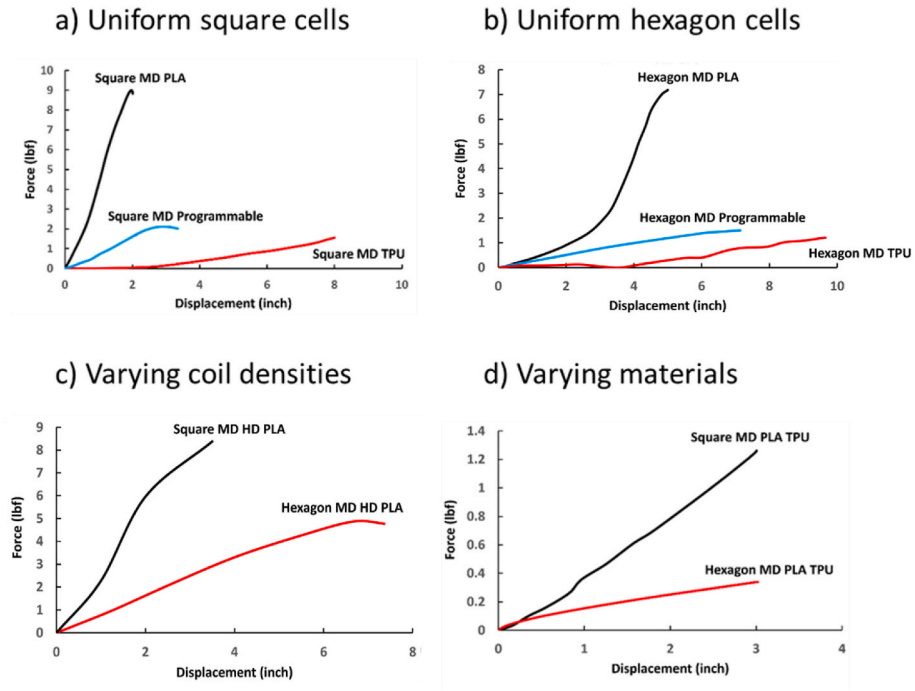

Fig. 19. Force-displacement curves for kerf structures under bending.

loading, which can enhance the load bearing and toughness of kerf structures.

5. Conclusion

We have investigated the interplay of mechanical behaviors of materials and microstructural topologies in controlling the flexibility,

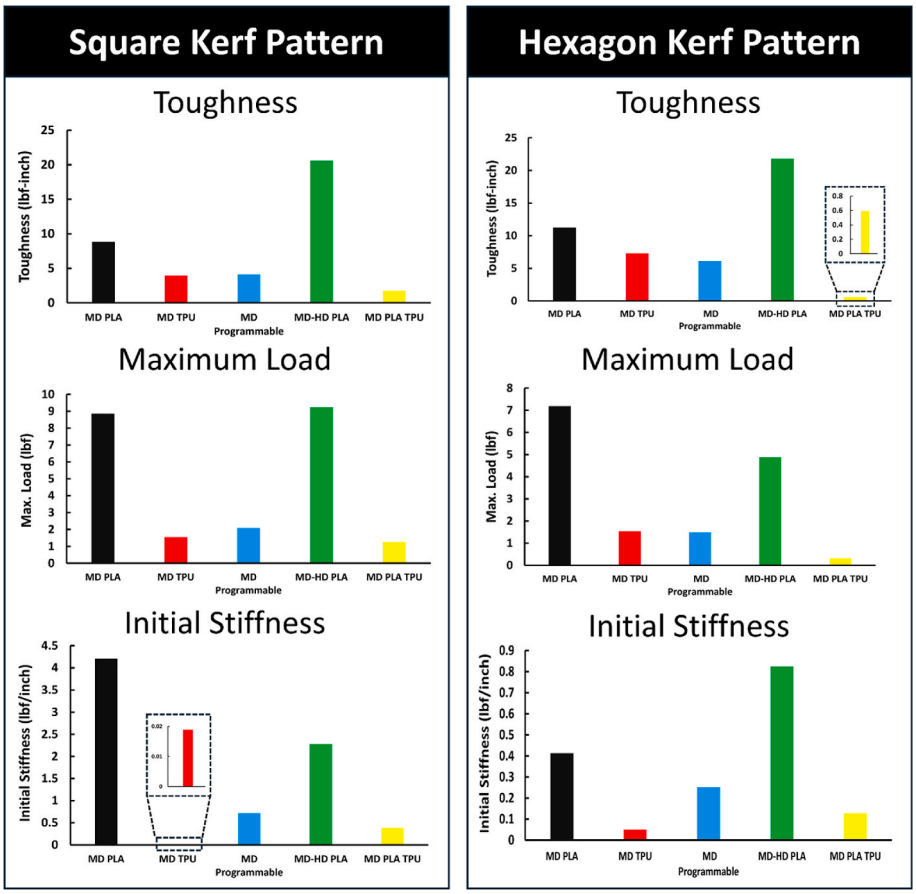

Fig. 20. Mechanical properties of kerf structures under bending for square and hexagon patterns. Top-to-bottom properties are initial stiffness, toughness, and maximum load.

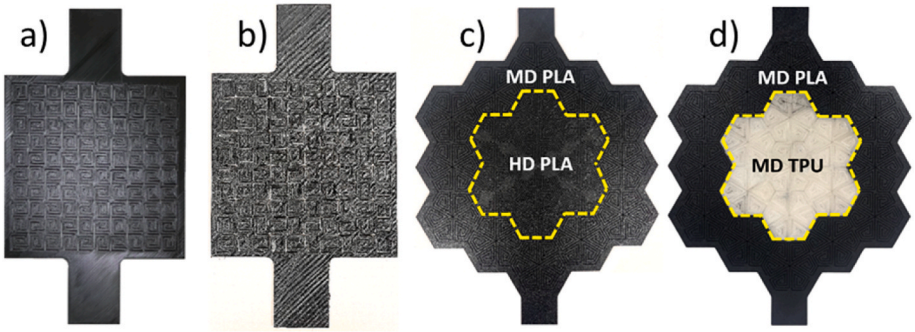

Fig. 21. Kerf structures for bending: a) square MD out of PLA; b) square LD programmable material; c) hexagon varying coil density MD-HD out of PLA; d) hexagonal MD with varying PLA-TPU material.

toughness, and load bearing of 3D-printed chiral kerf planar structures. We have considered two chiral kerf patterns, i.e., square and hexagon, with different coil densities and explored three materials, which are brittle PLA, soft TPU, and ductile programmable composite having PLA: TPU with a volume ratio of 50:50.

From purely geometrical parameters, the studied hexagon kerf cell has higher flexibility (lower stiffness) and extensibility (final displacement) compared to the square kerf cell. This is due to the higher slenderness ratios of beam segments that increase cell deformation and the higher total length of the beam segments that enable more cell uncoiling. The hexagon kerf cell has higher toughness compared to the square kerf cells, which is attributed to the higher geometric tortuosity that increases the load transfer pathways within cells in the hexagon kerf cells.

When using a relatively stiff material like brittle PLA or a relatively compliant material like TPU, the deformation mechanism of the kerf cells is governed in most part by the geometrical parameters of kerf cells. The brittle PLA limits the uncoiling of kerf cells, especially in those with lower coil density, resulting in low toughness. TPU kerf cells exhibit complete uncoiling; however, the compliant TPU causes low load bearing and toughness. The toughness, extensibility, and load bearing could be significantly improved by the combination of uncoiling and complex inelastic deformation of materials, which is the case of using a programmable composite. The initial deformation is governed by the elastic responses of the composite to initiate cell uncoiling. Further straining causes more cells to uncoil and material failure, i.e., sequential

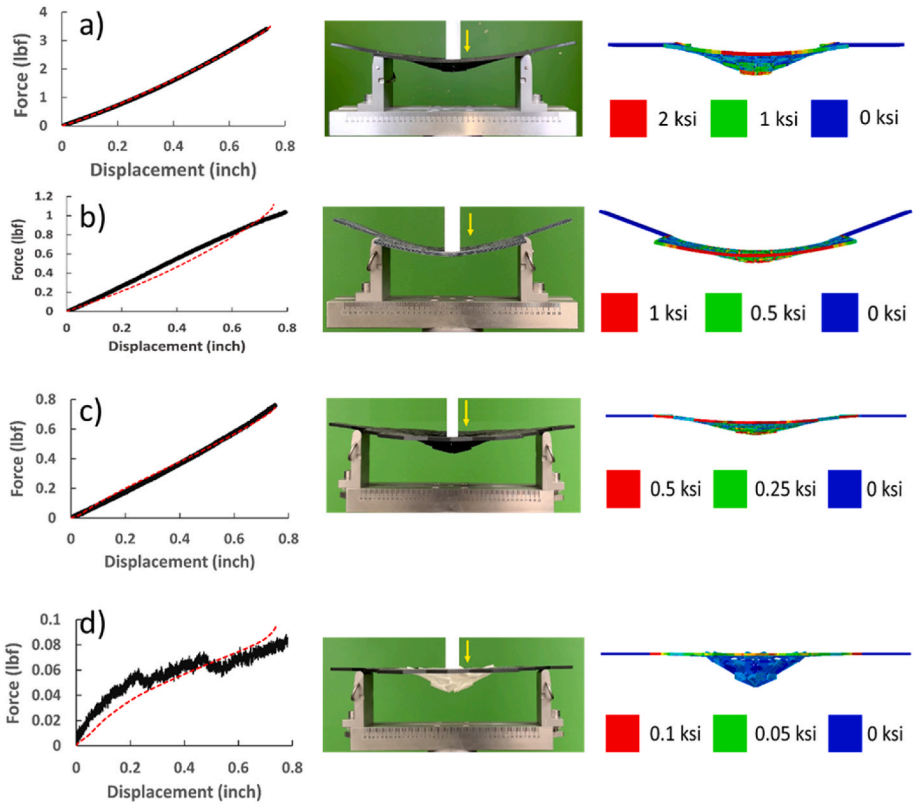

Fig. 22. Bending responses of kerf structures: a) square MD out of PLA; b) square LD programmable material; c) hexagon varying coil density MD-HD out of PLA; d) hexagonal MD with varying PLA-TPU material. Force-displacement curves (left), deformed shapes from experiment (middle), and von Mises stress contour from simulation (right).

load transfer from broken PLA to compliant TPU, altering the cross-sectional geometries of the beam segments. The changes in the cross-sectional geometries result in out-of-plane cell rotations.

We have studied kerf structures under uniaxial tension and bending. The ability of kerf cells to undergo reconfiguration, as a means to redistribute stresses, depends on the mechanical behavior of the materials. For example, uniaxial tensile loading induces shear banding in kerf structures with a square kerf pattern and ductile programmable composite, which is not seen in other materials and kerf structures with a hexagon kerf pattern. The shear banding is due to ductile shearing from continuous axial stress along the loading direction, which can be mitigated by breaking the stress continuity like in the hexagon pattern. Cell uncoiling delays failure, which can enhance load bearing, toughness, and extensibility. Using brittle material, while providing high stiffness, limits cell reconfigurations. The bending of kerf structures with relatively stiff materials such as PLA and programmable composite leads to cell packing from high resistant contact stresses among neighboring cells. Cell packing can result in enhancing load bearing and toughness under bending. Disrupting the uniform kerf topology with changing coil density or material enabled tuning the overall mechanical response and local stress magnitude and distribution, which can be used to delay failure and push the toughness and load-bearing ability of the structures.

The present study has provided some insights into the prominent feature of chiral kerf structures. Their coiled cells and kerf patterns lead to unconventional load transfer paths and cell reconfigurability with loading which are influenced by the mechanical behaviors of materials. This feature allows continuous stress redistribution to delay failure and improve loading resistance. We have demonstrated that in programmable composite kerf structures, the combination of cell reconfiguration and complex deformation of the composite enables tuning the overall mechanical responses of kerf structures to enhance load bearing, toughness, and final displacement. The kerf structures are promising for reconfigurable freeform structures, such as architectural façade, morphing structures, soft robotics, and implants.

CRediT authorship contribution statement

Aryabhat Darnal: Methodology, Software, Formal Analysis, Investigation, Validation, Data Curation, Writing – Original Draft. **Kanak Mantri:** Formal Analysis, Investigation, Data Curation. **Will Betts:** Investigation. **Jeeeun Kim:** Formal Analysis, Writing – Review & Editing. **Negar Kalantar:** Methodology, Software, Supervision. **Anastasia Muliana:** Writing – review & editing, Supervision, Investigation, Conceptualization.

Declaration of competing interest

The authors declare that they have no known competing financial interests or personal relationships that could have appeared to influence the work reported in this paper.

Data availability

Data will be made available on request.

Acknowledgment

We acknowledge the financial support of NSF grant CMMI 2222935. We thank the Texas A&M Super Computing Facility for computing resources.

Appendix A. Material Properties and Kinematic Representation of Kerf Cells

Three 3D printed materials, namely PLA, TPU, and programmable composite, are considered. The programmable filament has a parallel arrangement of PLA and TPU layers, see Figure A1. PLA is brittle and has relatively high stiffness and strength, while TPU is compliant with low load-bearing ability. The filaments used in this study were manufactured by OVERTURE 3D. The printing parameters were chosen as suggested by the manufacturer, see Table A1.

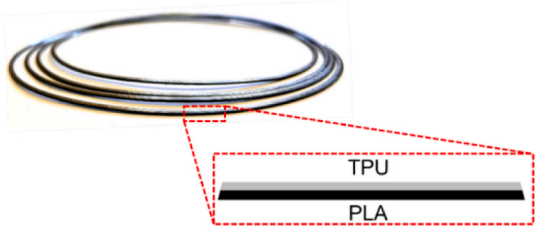

Fig. A1. Programmable filament with TPU top layer and PLA bottom layer

Table A1
Printing process parameters of kerf unit cells with different materials

Process Parameters	PLA	TPU	PLA:TPU
Print Temperature (°C)	210	220	235
Bed Temp (°C)	60	60	60
Print Speed (mm/s)	40	20	30
Infill Density (%)	100	100	100
Flowrate (%)	100	100	100
Layer Height (mm)	0.2	0.2	0.2
Raster Angle	45°	45°	45°

The kinematic representation of the beam elements is shown in Fig. A2. The x-axis is in the axial direction, and the y and z axes are in the lateral direction (in the local coordinate). The deformations in the beam segments are classified as in-plane bending (x-y plane), out-of-plane bending (x-z plane), transverse shearing in in-plane and out-of-plane, and axial stretching in the x-axis.

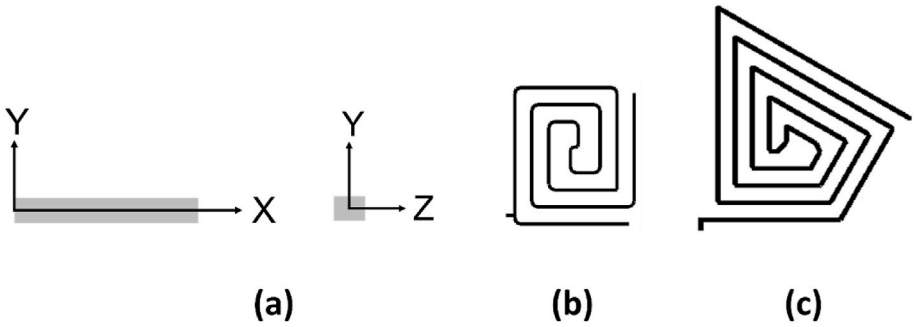

Fig. A2. Modeling kerf unit cell: a) Kinematic representation of the cross-sectional area of the beam element, b) Square kerf cell, c) Hexagon kerf cell.

Appendix B. Mechanical Properties of Kerf Cells

The mechanical properties, namely toughness, maximum load capacity, final displacement, and initial stiffness of square and hexagon kerf cells for all three materials are listed in Table B1.

Table B1
Mechanical properties of kerf unit cells with different materials

Geometry	Material	Cut Density	Toughness (lbf-in.)	Max. Load (lbf)	Final Displacement (in.)	Initial Stiffness (lbf/in.)
Square	PLA	LD	5.67 ± 0.83	30.67 ± 1.05	0.27 ± 0.03	225.46 ± 5.31
		MD	3.53 ± 0.09	9.15 ± 0.20	0.62 ± 0.04	28.94 ± 1.68
		HD	3.56 ± 0.63	3.86 ± 0.12	1.29 ± 0.32	7.44 ± 0.28
	TPU	LD	4.96 ± 0.16	5.39 ± 0.17	1.84 ± 0.11	2.28 ± 0.03
		MD	4.59 ± 0.66	2.82 ± 0.40	4.96 ± 0.06	0.27 ± 0.02
		HD	1.72 ± 0.19	1.03 ± 0.07	5.92 ± 0.14	0.10 ± 0.006
	Programmable	LD	14.36 ± 2.46	12.25 ± 1.87	1.65 ± 0.06	75.57 ± 9.69
		MD	21.23 ± 1.90	9.73 ± 0.39	4.36 ± 0.12	10.78 ± 0.89

(continued on next page)

Table B1 (*continued*)

Geometry	Material	Cut Density	Toughness (lbf-in.)	Max. Load (lbf)	Final Displacement (in.)	Initial Stiffness (lbf/in.)
		HD	16.18 ± 1.99	7.03 ± 2.52	5.59 ± 0.25	3.91 ± 0.54
Hexagon	PLA	LD	5.58 ± 0.20	12.74 ± 0.29	0.73 ± 0.05	32.03 ± 0.77
		MD	4.41 ± 0.67	4.41 ± 0.67	1.61 ± 0.37	6.04 ± 1.89
		HD	4.43 ± 0.11	1.57 ± 0.03	3.94 ± 0.40	1.04 ± 0.14
	TPU	LD	16.68 ± 0.10	11.07 ± 0.38	9.03 ± 0.06	0.23 ± 0.01
		MD	4.16 ± 0.79	1.03 ± 0.10	13.95 ± 0.11	0.05 ± 0.004
		HD	1.47 ± 0.25	0.88 ± 0.09	18.43 ± 0.79	0.01 ± 0.0007
	Programmable	LD	74.81 ± 4.26	18.37 ± 2.93	6.84 ± 1.10	19.97 ± 0.94
		MD	67.46 ± 3.68	16.86 ± 1.28	13.07 ± 0.44	3.38 ± 0.22
		HD	40.05 ± 1.99	5.87 ± 1.32	16.97 ± 0.57	2.29 ± 0.21

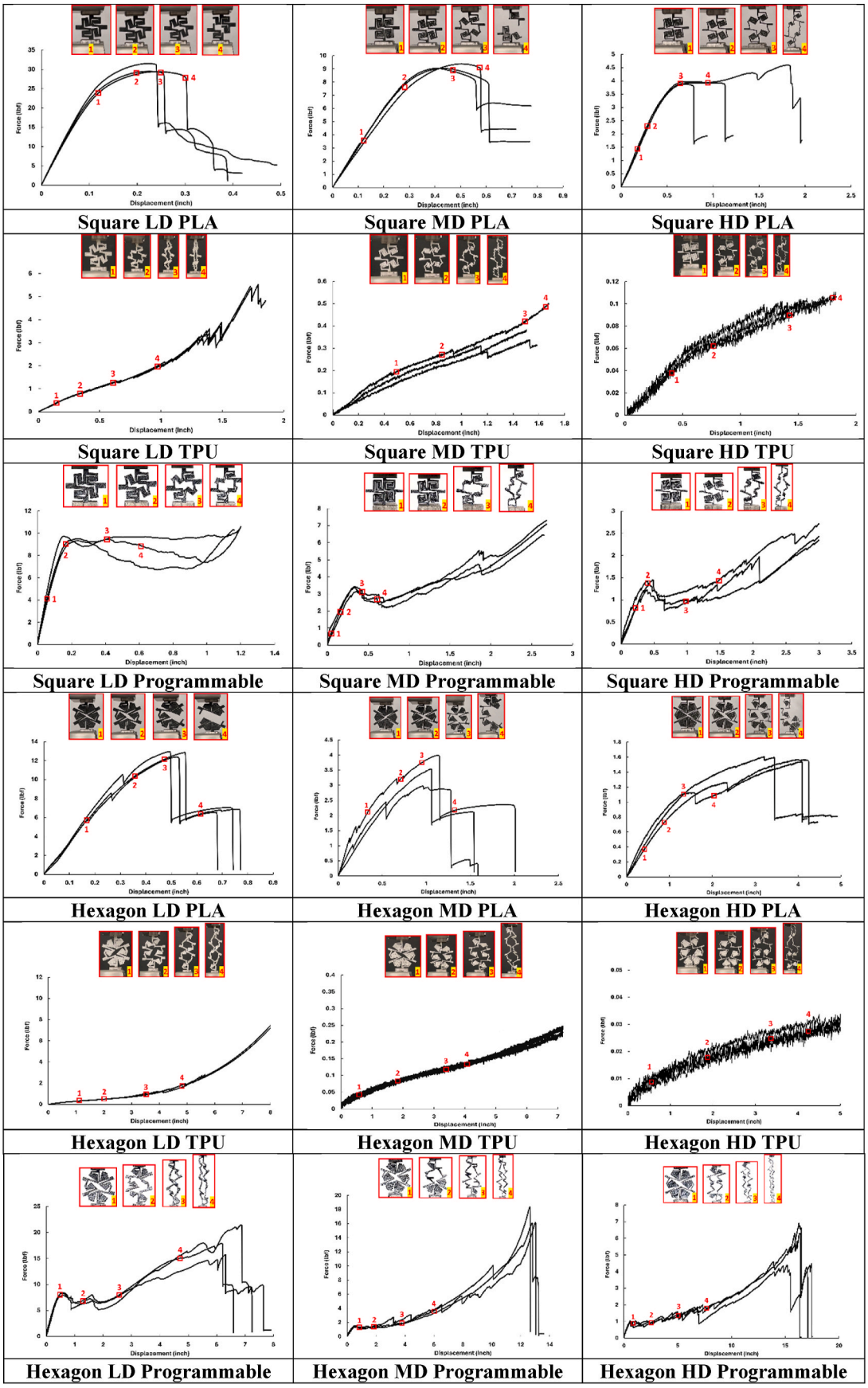

Fig. B1. Correlation between deformed shapes and force-displacement responses for square and hexagon kerf cells for PLA, TPU and Programmable material.

Appendix C. Finite Element Analyses of Kerf Cells

Figure C1 shows the beam element models of kerf cells. The square unit cells mesh with LD, MD, and HD consisted of 353, 532 and 732 elements, respectively, and the hexagon unit cells mesh consisted of 648, 961, 1177 elements, respectively. One arm of the unit cell was fixed, and an axial displacement was prescribed at the opposite arm. We modeled PLA as a linear elastic and isotropic material, TPU as a hyperelastic incompressible material following the Yeoh constitutive model with a strain energy function $W = \sum_{i=1}^{3} C_{i0}(I_1 - 3)^i$, and the programmable composite as elastic-plastic material. The elastic modulus and Poisson's ratio for the PLA are 522 ksi and 0.3, respectively, [50]. For capturing the brittle failure of the PLA, we considered material softening. The ultimate (complete failure) stress of PLA is 8.8 ksi [50] and the stiffness reduction starts at 7.2 ksi stress. For the programmable composite, the elastic modulus, Poisson's ratio, and yield stress are 261 ksi, 0.35, and 3 ksi, respectively. The Yeoh material parameters C_{10}, C_{20}, and C_{30} for the TPU are 1121.621 psi, −230.980 psi, and 26.887 psi, respectively. The computational time to simulate the uniaxial tension for all kerf cells varied between 5 and 25 s.

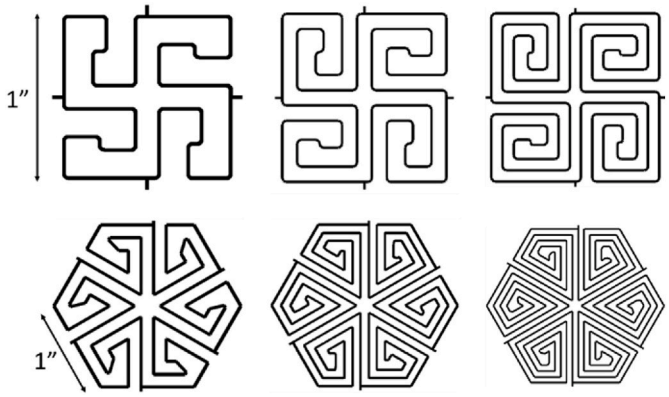

Fig. C1. Models for LD, MD, and HD square and hexagon kerf cells using beam elements.

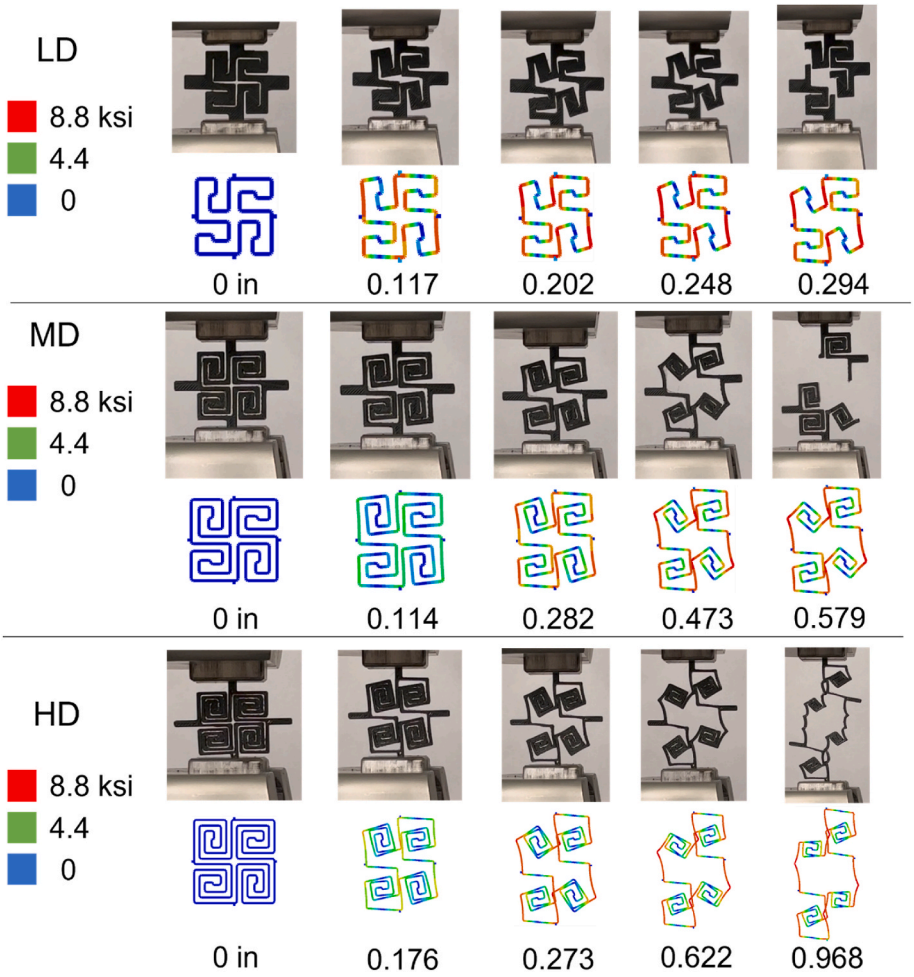

Fig. C2. Deformed shapes of square PLA kerf cells of various cut densities

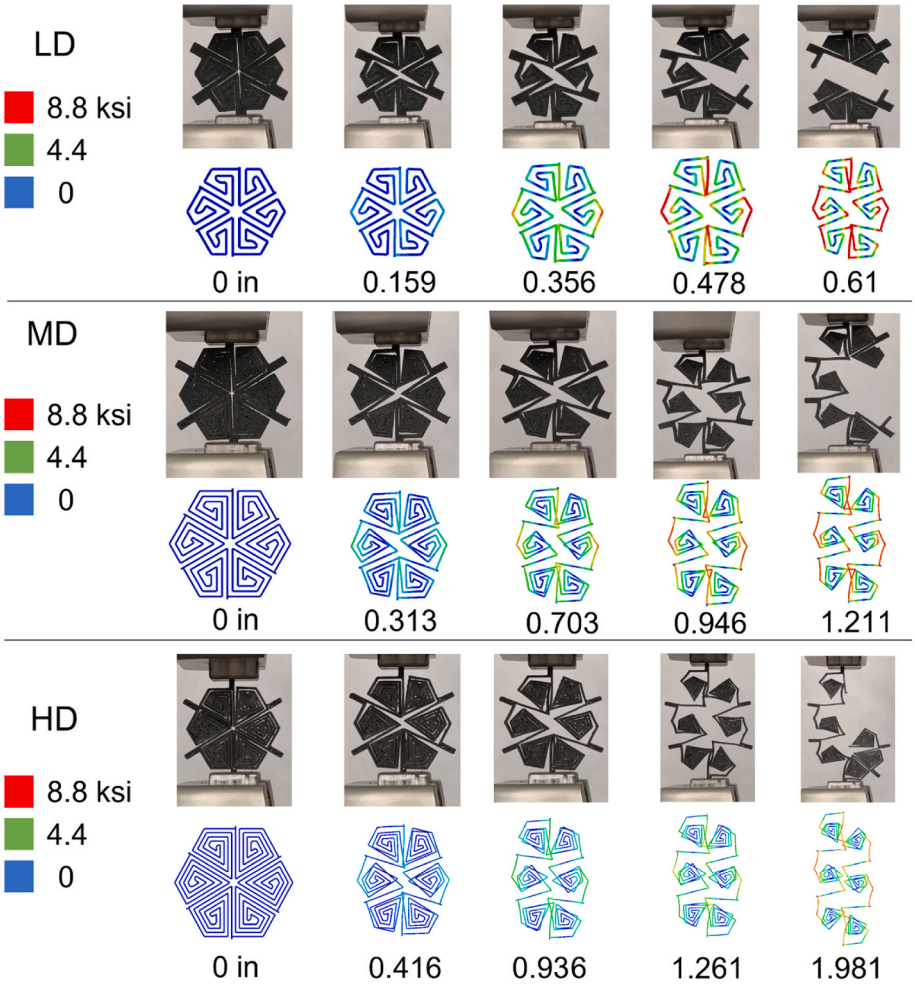

Fig. C3. Deformed shapes of hexagon PLA kerf cells of various cut densities

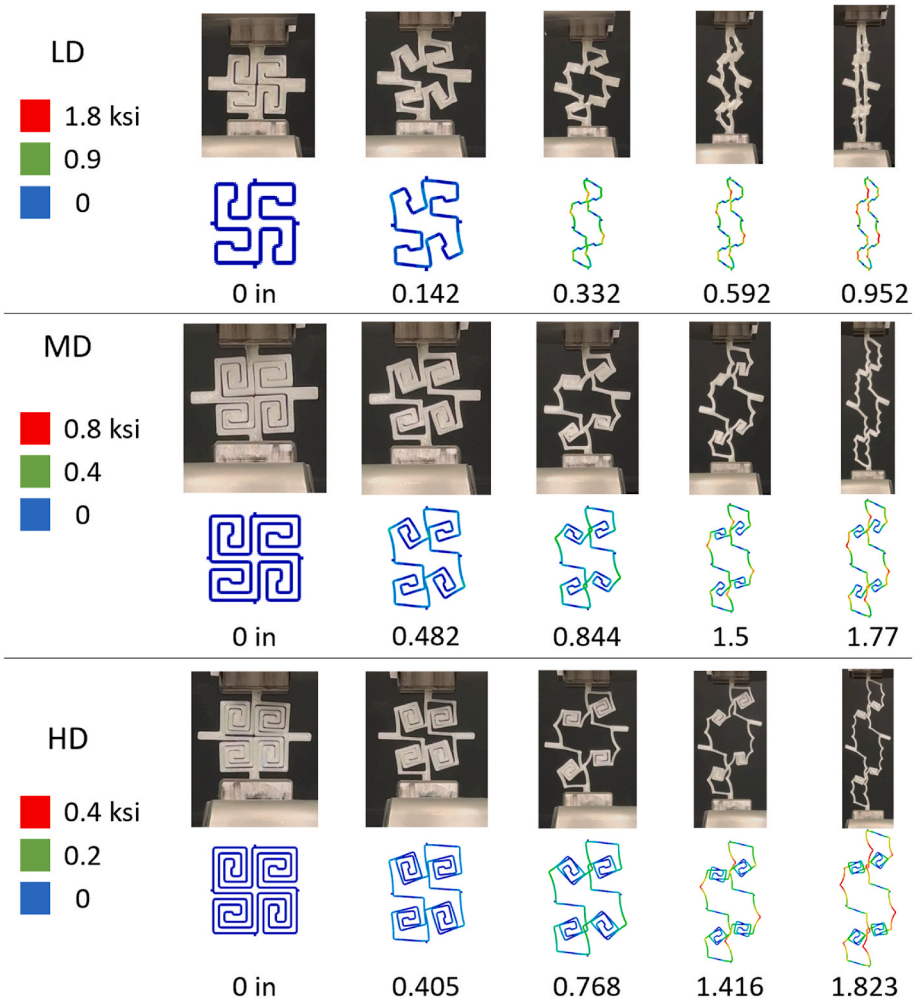

Fig. C4. Deformed shapes of square TPU kerf cells of various cut densities

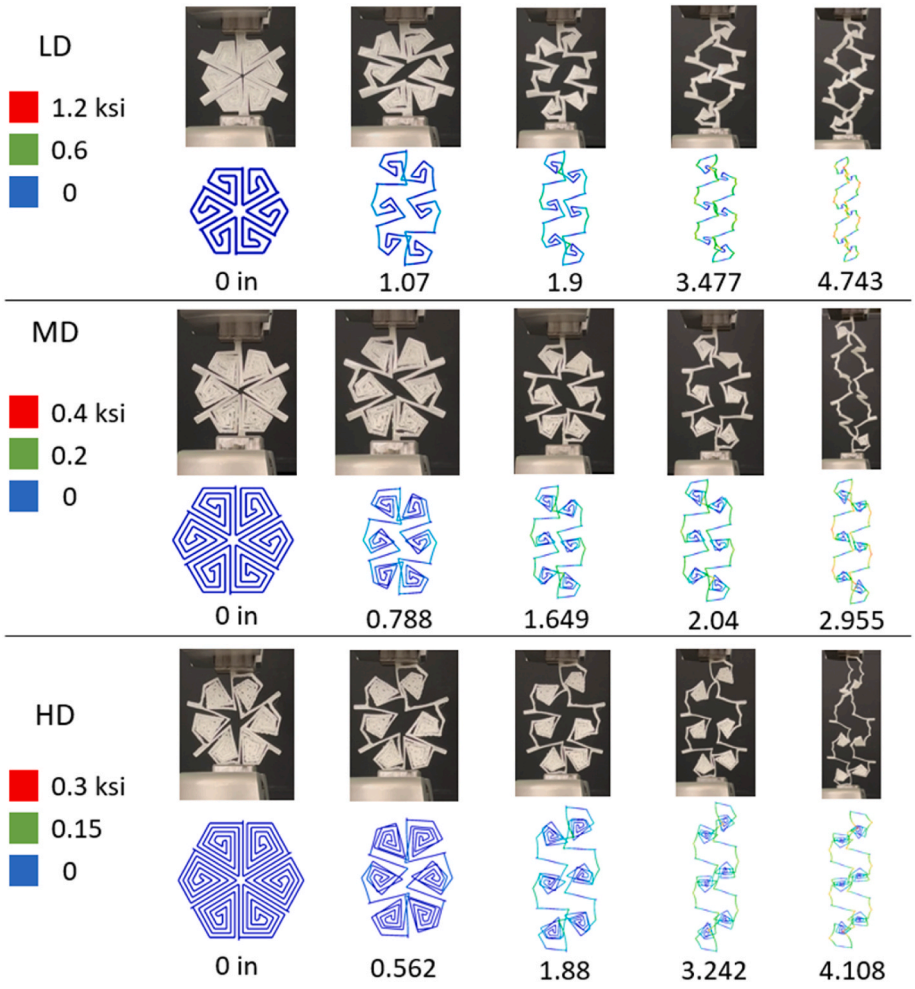

Fig. C5. Deformed shapes of hexagon TPU kerf cells of various cut densities

Fig. C6. Changes in the microstructure of TPU square (top) and hexagon (bottom) kerf cell during loading-unloading

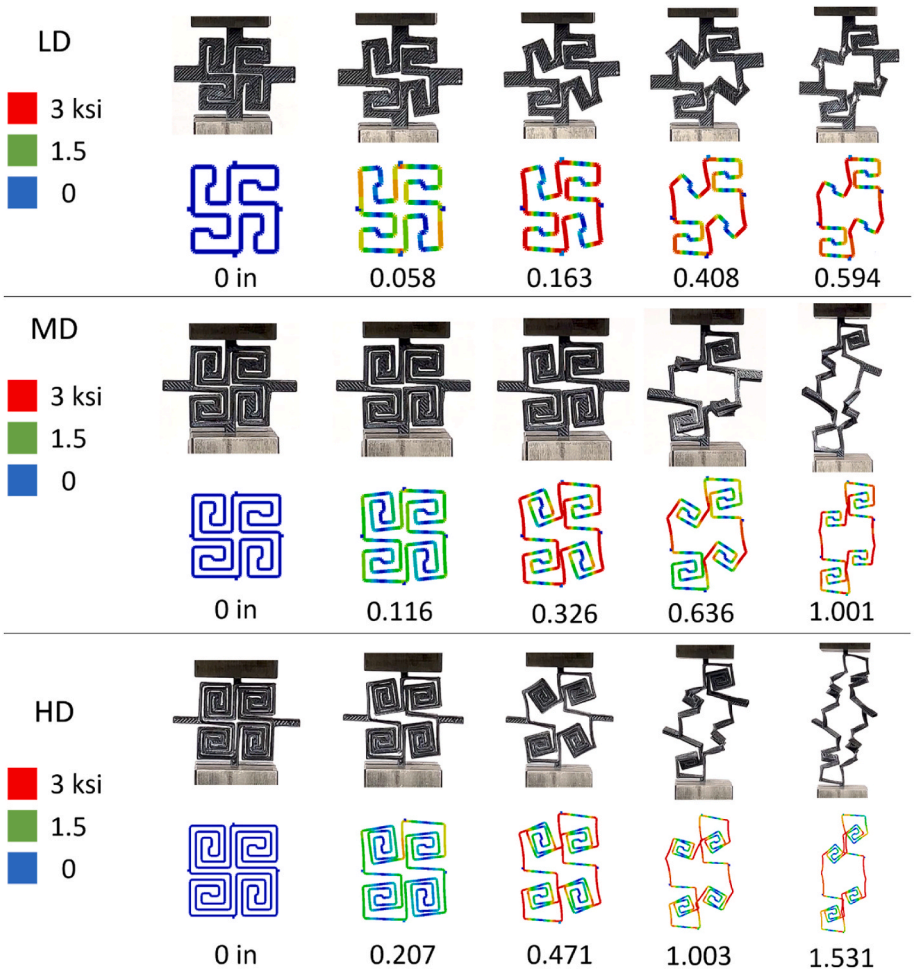

Fig. C7. Deformed shapes of square programmable kerf cells of various cut densities

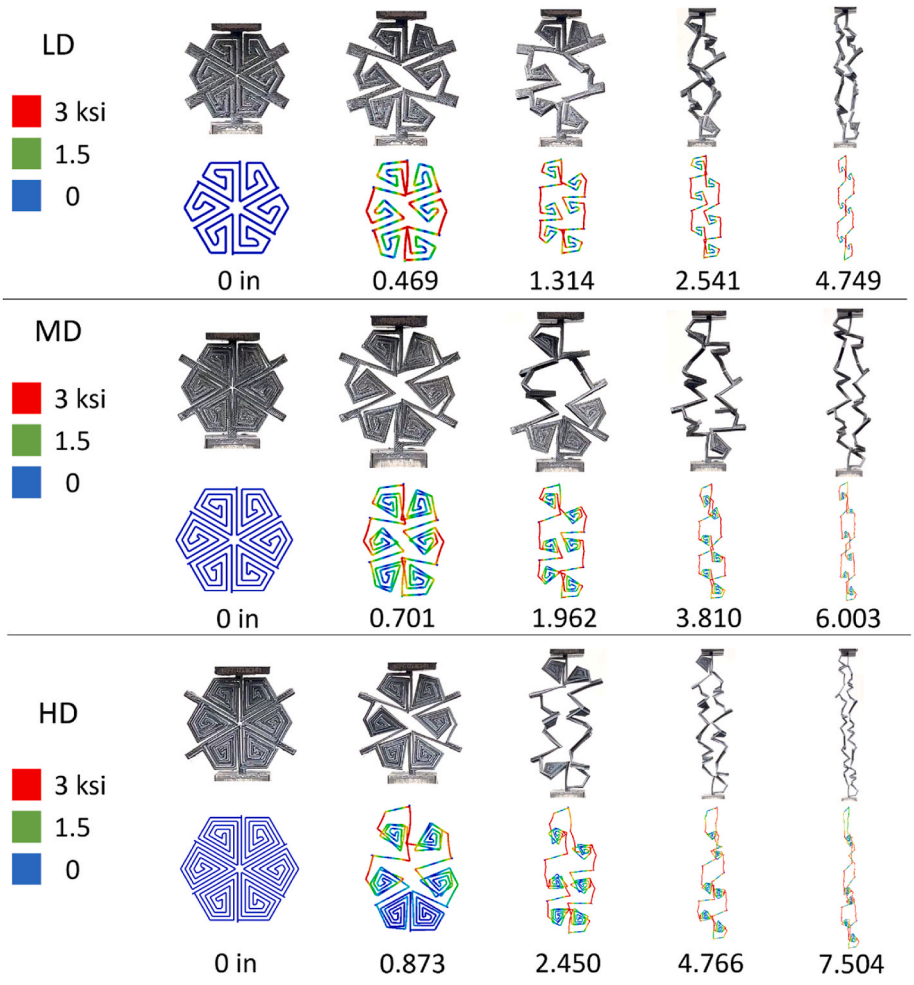

Fig. C8. Deformed shapes of hexagon programmable kerf cells of various cut densities

Appendix D. Kerf Structures Under Tension and Bending

This Appendix summarizes responses of kerf structures under uniaxial tension and bending. Figure D1 shows the overall force-displacement results from uniaxial tensile simulations.

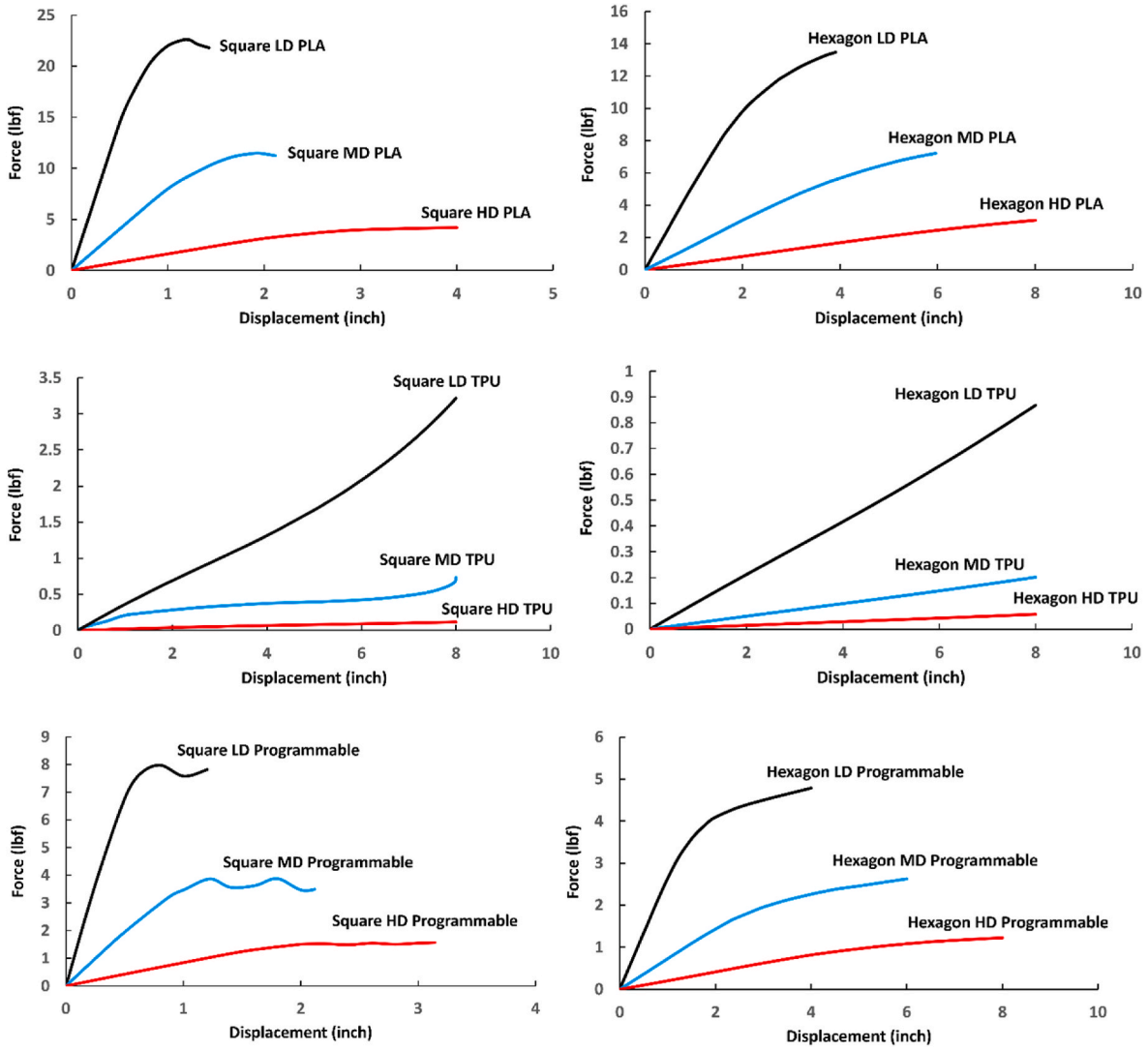

Fig. D1. Uniaxial tensile force-displacement curves of kerf structures with uniform coil densities for square (left) and hexagon (right) patterns with PLA (top), TPU (middle) and programmable material (bottom)

Figures D2 and **D3** display deformed shapes comparing experimental and simulation results for selected kerf structures with square and hexagon patterns, respectively, under uniaxial tension. For the kerf structures with a uniform coil density, i.e. Figs. D2a, **D3a**, and **D3b**, there is a uniform uncoiling of the beam segments throughout the kerf structures whereas for the kerf structures with varying coil density, e.g., Fig. D2b, the HD region undergoes the uncoiling first and the failure stress occurred in this region as evident by the stress contour while the MD region undergoes much lower stresses and negligible deformations. For the kerf structure with varying material, e.g., Fig. D3c, only the TPU region of the kerf panel undergoes deformations, owing to the significantly low stiffness of the TPU when compared to the one of the PLA.

In case of the kerf structure with a square uniform coil density out of a programmable composite, the plastic deformation in a narrow region of the kerf structure caused shear banding, followed by the in-plane cell rotation and uncoiling in this region. The experiment also indicated out-of-plane rotation (bending) of kerf cell in addition to uncoiling which is not captured by the simulation. The out of plane rotation of the programmable kerf structure is due to the heterogenous material failure of the programmable composite. Under the tensile force, the PLA part of the programmable polymer breaks while the presence of TPU prevents cell breakage and allows for continuous deformations. The overall response of the programmable compiste is modeled as a homogeneous plastic deformation ignoring its heterogeneity nature.

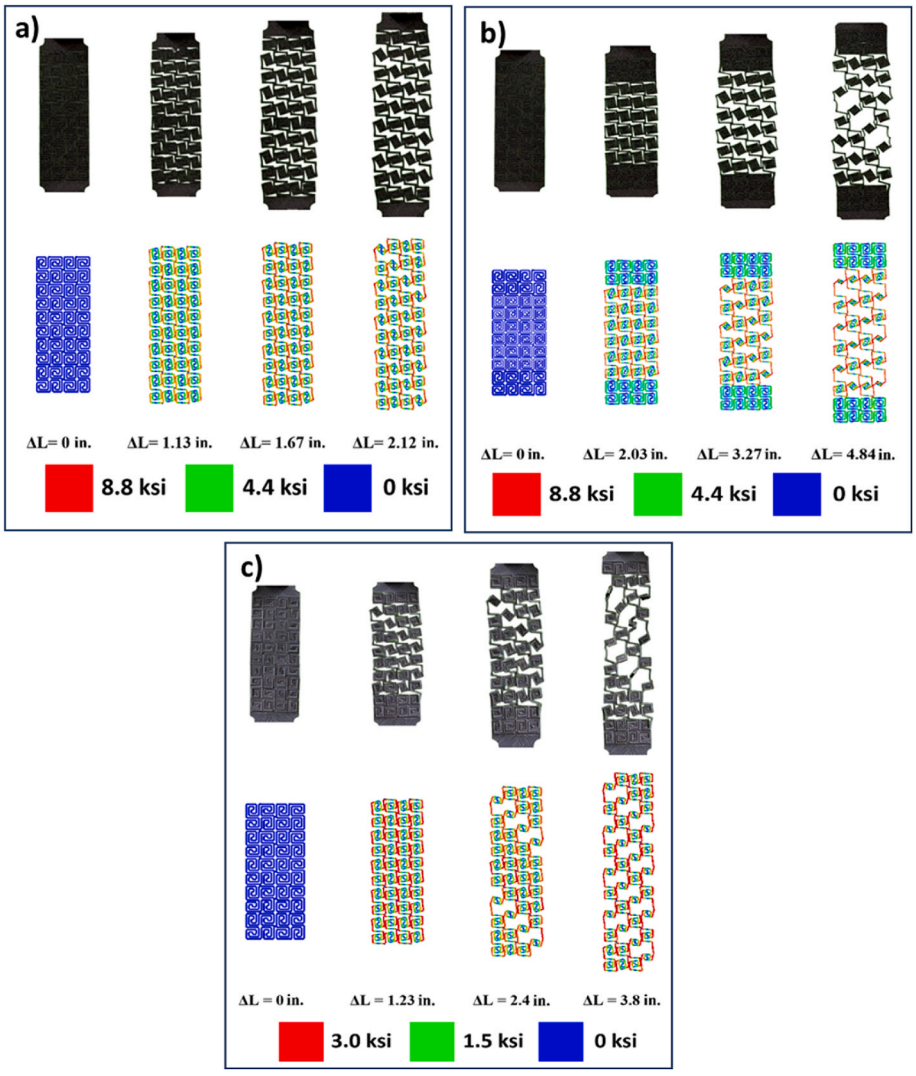

Fig. D2. Deformed shape of experiment and simulation of kerf structures with square kerf pattern under uniaxial tensile force: a) MD of PLA; b) MD-HD of PLA, and c) MD programmable polymer

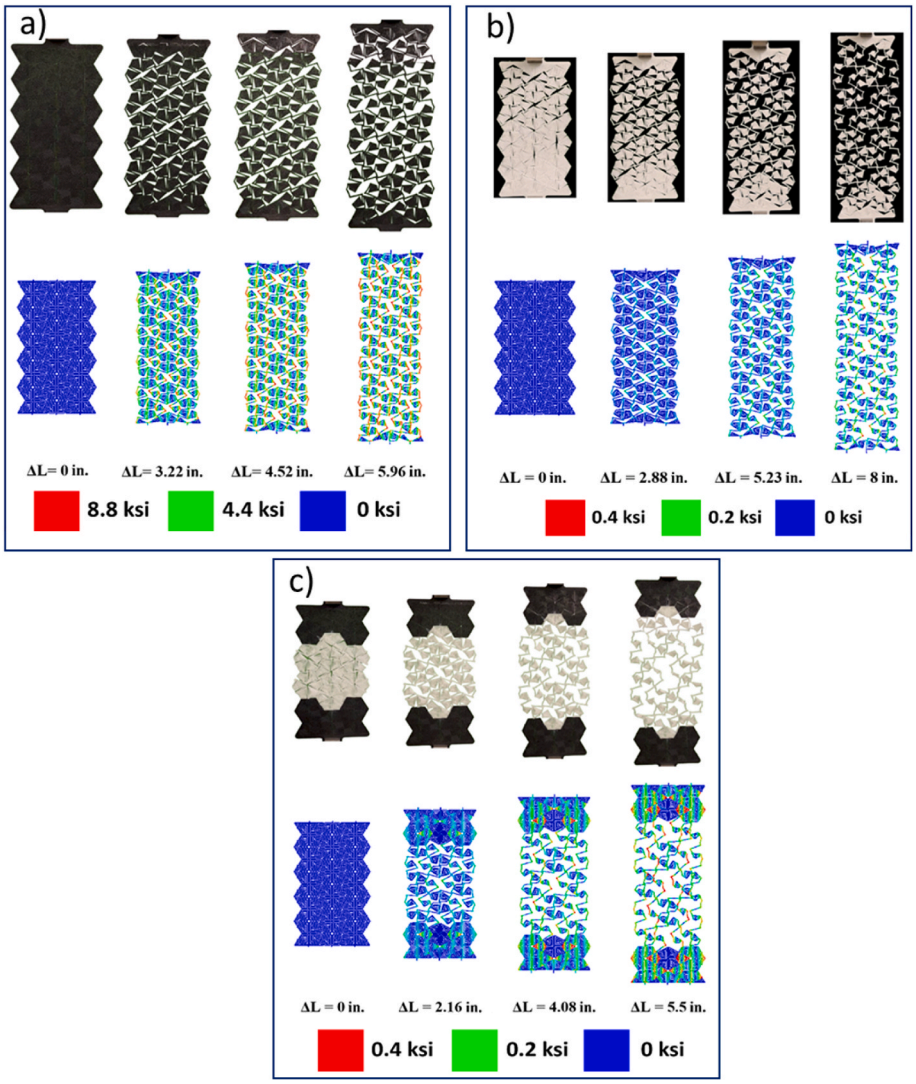

Fig. D3. Deformed shape of experiment and simulation of kerf structures with hexagon kerf pattern under uniaxial tensile force. a) MD PLA, b) MD TPU, and c) MD PLA TPU

For the bending analyses, the kerf structures were meshed with quadratic B31 beam elements, depicted in Figure D4. The indenter and supports were meshed with linear hex-dominated 8-node bricked solid elements (C38DR). The indenter had 16 elements, and the supports had 1863 elements. A general contact model based on Coulomb friction was defined with a frictional penalty coefficient of 0.4 along the tangential directions, as well as a hard normal contact. Support 1 and 2 were fixed in all degree of freedoms (no translation and rotation) and a displacement of 0.75 inches in negative y-direction was applied to the indenter. The arrow on the indenter indicated the direction of displacement.

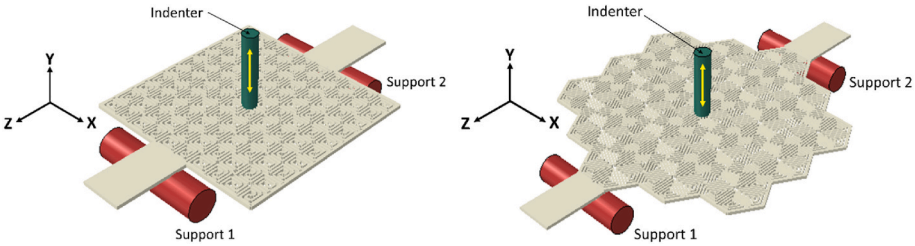

Fig. D4. Finite element model of the kerf structures with square (left) and hexagon (right) patterns under three-point bending test setup.

The bending responses are depicted in Fig. D5 and the corresponding deformed shapes for kerf structures with medium coil density are shown in Figs. D6 - D9.

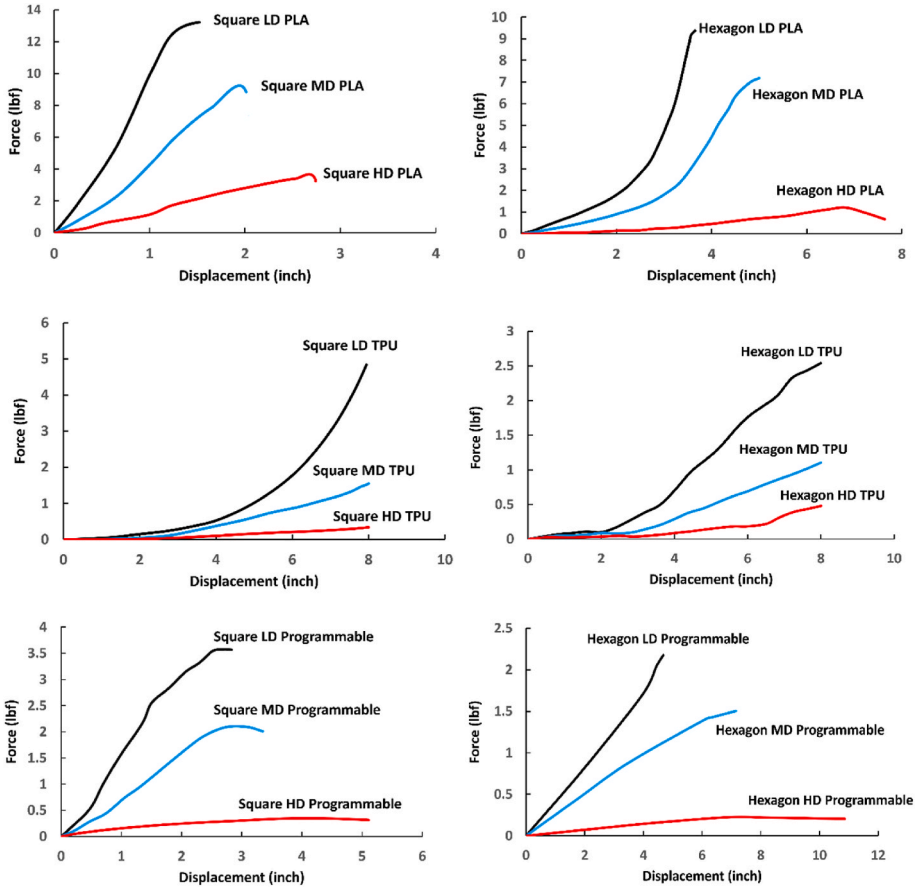

Fig. D5. Bending force-displacement curves of kerf structures with uniform coil densities for square (left) and hexagon (right) patterns with PLA (top), TPU (middle) and programmable material (bottom)

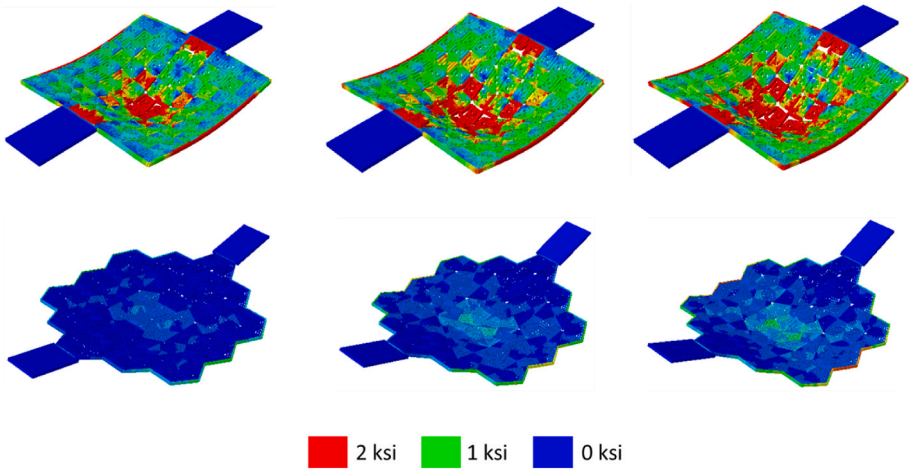

Fig. D6. Bending behavior of kerf structure with uniform medium coil density for square and hexagon pattern with PLA material.

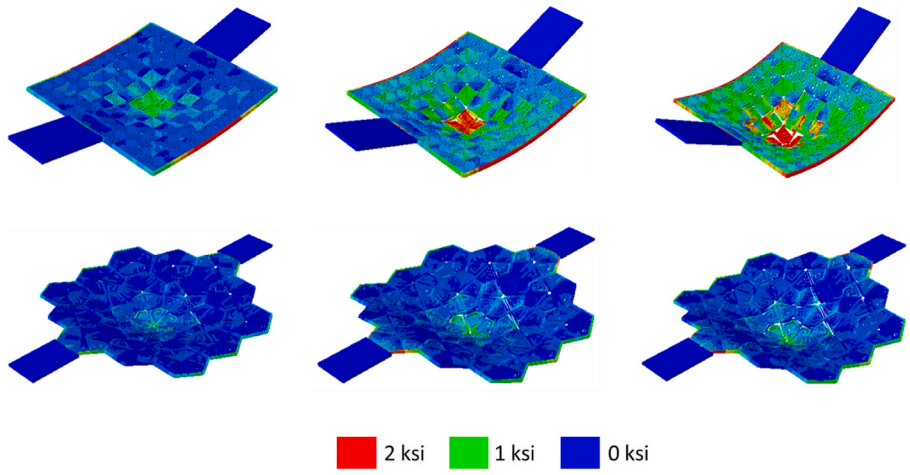

Fig. D7. Bending behavior of kerf structure with medium-high coil density for square and hexagon pattern with PLA material.

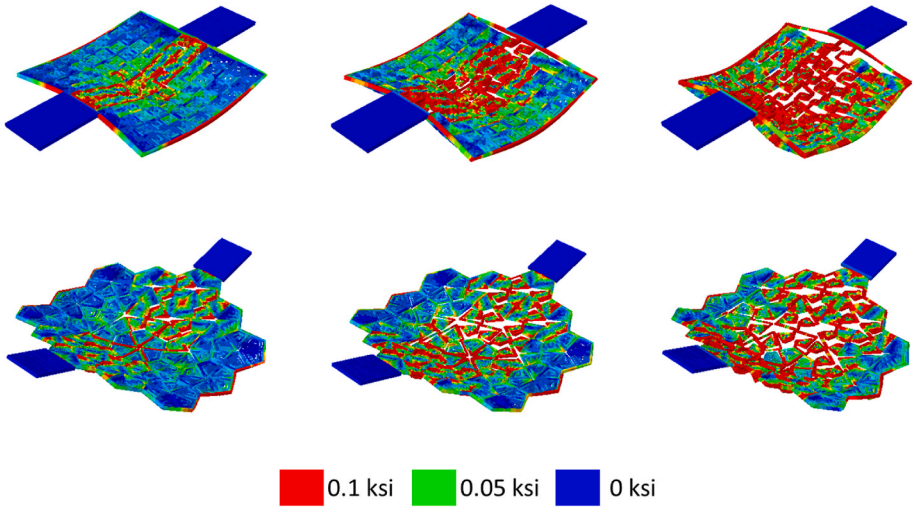

Fig. D8. Bending behavior of kerf structure with uniform medium coil density for square and hexagon pattern with TPU material.

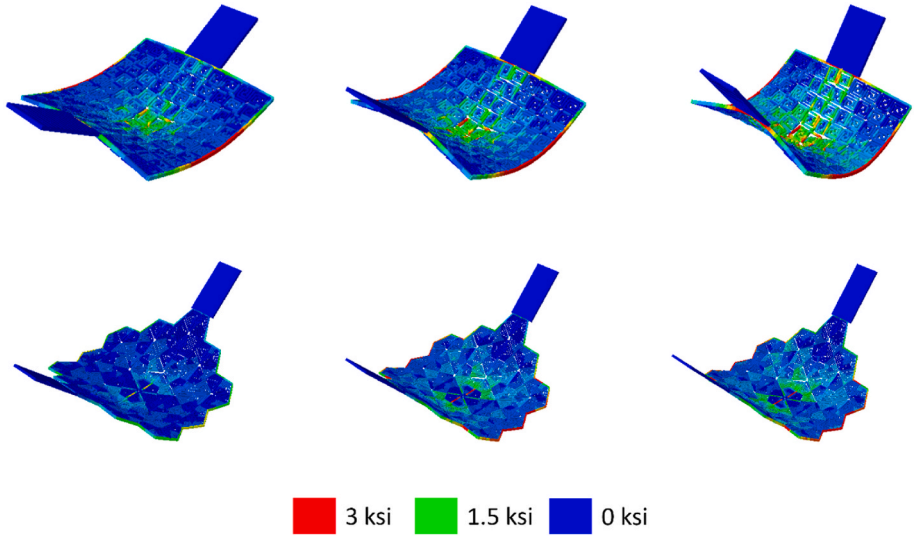

Fig. D9. Bending behavior of kerf structure with uniform medium coil density for square and hexagon pattern with programmable material.

References

[1] Jiang C, Wang J, Wallner J, Pottmann H. Freeform honeycomb structures, computer graphics forum. Wiley Online Library; 2014. p. 185–94.
[2] Taminger K, Hafley RA, Dicus DL. Solid freeform fabrication: an enabling technology for future space missions. 2002 international conference on metal powder deposition for rapid manufacturing. 2002.
[3] Chen S, Tan WS, Bin Juhari MA, Shi Q, Cheng XS, Chan WL, Song J. Freeform 3D printing of soft matters: recent advances in technology for biomedical engineering. Biomed. Eng. Letters 2020;10(4):453–79.
[4] Kim K, Son K, Kim E-D, Kim S. Current trends and future directions of free-form building technology. Architect Sci Rev 2015;58(3):230–43.
[5] Prithipaul PK, Kokkolaras M, Pasini D. Assessment of structural and hemodynamic performance of vascular stents modelled as periodic lattices. Med Eng Phys 2018; 57:11–8.
[6] Douglas GR, Phani AS, Gagnon J. Analyses and design of expansion mechanisms of balloon expandable vascular stents. J Biomech 2014;47(6):1438–46.
[7] Jiang H, Ziegler H, Zhang Z, Zhang H, Le Barbenchon L, Atre S, Chen Y. 3D printed tubular lattice metamaterials for mechanically robust stents. Compos B Eng 2022; 236:109809.
[8] Tan G, Duan X, Niu D, Ma J. Visual synthesis of uniaxial synchronous deployment mechanisms for solid-surface deployable antennas. Mech Mach Theor 2022;178: 105073.
[9] Sakovsky M, Pellegrino S, Constantine J. Rapid deployable antenna concept selection for cubesats. 2016. Cal Tech.
[10] Meguro A, Shintate K, Usui M, Tsujihata A. In-orbit deployment characteristics of large deployable antenna reflector onboard Engineering Test Satellite VIII. Acta Astronaut 2009;65(9–10):1306–16.
[11] Shahid Z, Bond CG, Johnson MS, Hubbard Jr JE, Kalantar N, Muliana A. Dynamic response of flexible viscoelastic kerf structures of freeform shapes. Int J Solid Struct 2022:111895.
[12] Shahid Z, Hubbard JE, Kalantar N, Muliana A. An investigation of the dynamic response of architectural kerf structures. Acta Mech 2022:1–25.
[13] Lingling C, Qi L, Feng G, Xintian D, Yuqing H, Yangchen D. Design, modeling, and control of morphing aircraft: a review. Chin J Aeronaut 2022;35(5):220–46.
[14] Sun J, Guan Q, Liu Y, Leng J. Morphing aircraft based on smart materials and structures: a state-of-the-art review. J Intell Mater Syst Struct 2016;27(17): 2289–312.
[15] Haifeng P, Erbao D, Shiwu Z, Jie Y. Research on flexible honeycomb structure design for morphing aircraft. In: Proceedings of 2011 international conference on electronic & mechanical engineering and information technology; 2011. p. 2271–4. IEEE.
[16] Callens SJ, Zadpoor AA. From flat sheets to curved geometries: origami and kirigami approaches. Mater Today 2018;21(3):241–64.
[17] Zirbel SA, Lang RJ, Thomson MW, Sigel DA, Walkemeyer PE, Trease BP, Magleby SP, Howell LL. Accommodating thickness in origami-based deployable arrays. J Mech Des 2013;135(11).
[18] Chen Y, Peng R, You Z. Origami of thick panels. Science 2015;349(6246):396–400.
[19] Lang RJ, Nelson T, Magleby S, Howell L. Thick rigidly foldable origami mechanisms based on synchronized offset rolling contact elements. J Mech Robot 2017;9(2):021013.
[20] Peraza-Hernandez EA, Hartl DJ, Malak Jr RJ, Lagoudas DC. Origami-inspired active structures: a synthesis and review. Smart Mater Struct 2014;23(9):094001.
[21] Li Y, Zhang Q, Hong Y, Yin J. 3D transformable modular Kirigami based programmable metamaterials. Adv Funct Mater 2021;31(43):2105641.
[22] Wang Y, Wang C. Buckling of ultrastretchable kirigami metastructures for mechanical programmability and energy harvesting. Int J Solid Struct 2021;213: 93–102.
[23] Pishvar M, Harne RL. Foundations for soft, smart matter by active mechanical metamaterials. Adv Sci 2020;7(18):2001384.
[24] Cui H, Yao D, Hensleigh R, Lu H, Calderon A, Xu Z, Davaria S, Wang Z, Mercier P, Tarazaga P. Design and printing of proprioceptive three-dimensional architected robotic metamaterials. Science 2022;376(6599):1287–93.
[25] Ebrahimi MS, Noruzi M, Hamzehei R, Etemadi E, Hashemi R. Revolutionary auxetic intravascular medical stents for angioplasty applications. Mater Des 2023; 235:112393.
[26] Wu W, Hu W, Qian G, Liao H, Xu X, Berto F. Mechanical design and multifunctional applications of chiral mechanical metamaterials: a review. Mater Des 2019;180: 107950.
[27] Darnal A, Shahid Z, Han J, Moreno M, Muliana A. Viscoelastic responses of MDF kerf structures. Proceedings of the American society for composites—thirty-sixth technical conference on composite materials. 2021.
[28] Darnal A, Mantri K, Shahid Z, Kalantar N, Muliana A. The influence of inelastic materials on freeform kerf structures. Thin-Walled Struct 2023:111292.
[29] Zhang W, Neville R, Zhang D, Scarpa F, Wang L, Lakes R. The two-dimensional elasticity of a chiral hinge lattice metamaterial. Int J Solid Struct 2018;141: 254–63.
[30] Holterman A. Pattern Kerfing for Responsive Wooden Surfaces: a formal approach to produce flexible panels with acoustic performance. 2018.
[31] Liu D, Shahid Z, Tung Y-H, Muliana A, Ham Y, Kalantar N, Chaspari T, Green E, Hubbard JE. Tunable acoustic properties in reconfigurable kerf structures. J Architect Eng 2023;29(3):04023018.
[32] Bohrani A KN, Muliana A, Shahid Z, Rezaei E, Green E. The sound of kerfing: a new approach to integrating geometry, materials, and acoustics to build invisibles. Proceedings ACADIA 2022 hybrids and haecceities. Philadelphia, PA: University of Pennsylvania; 2022.
[33] Boley JW, Van Rees WM, Lissandrello C, Horenstein MN, Truby RL, Kotikian A, Lewis JA, Mahadevan L. Shape-shifting structured lattices via multimaterial 4D printing. Proc Natl Acad Sci USA 2019;116(42):20856–62.
[34] Airoldi A, Bettini P, Zazzarini M, Scarpa F. Failure and energy absorption of plastic and composite chiral honeycombs. Struct. Shock Impact XII 2012;126:101–14.
[35] Forte AE, Melancon D, Zanati M, De Giorgi M, Bertoldi K. Chiral mechanical metamaterials for tunable optical transmittance. Adv Funct Mater 2023:2214897.
[36] Frenzel T, Kadic M, Wegener M. Three-dimensional mechanical metamaterials with a twist. Science 2017;358(6366):1072–4.
[37] Zhang Z, Scarpa F, Bednarcyk BA, Chen Y. Harnessing fractal cuts to design robust lattice metamaterials for energy dissipation. Addit Manuf 2021;46:102126.
[38] Wang D, Dong L, Gu G. 3D printed fractal metamaterials with tunable mechanical properties and shape reconfiguration. Adv Funct Mater 2023;33(1):2208849.
[39] Lu Q, Darnal A, Takahashi H, Muliana AH, Kim J. User-centered property adjustment with programmable filament. CHI conference on human factors in computing systems. Extended Abstracts; 2022. p. 1–6.
[40] Darnal A, Shahid Z, Deshpande H, Kim J, Muliana A. Tuning mechanical properties of 3D printed composites with PLA: TPU programmable filaments. Compos Struct 2023:117075.
[41] Darnal A, Mantri K, Kim J, Kalantar N, Muliana A. Tuning mechanical response of hierarchical composite structures. Proceeding of the American society of composites-38th technical conference. 2023.
[42] Chen R, Turman C, Jiang M, Kalantar N, Moreno M, Muliana A. Mechanics of kerf patterns for creating freeform structures. Acta Mech 2020;231(9):3499–524.
[43] Zarrinmehr S, Ettehad M, Kalantar N, Borhani A, Sueda S, Akleman E. Interlocked archimedean spirals for conversion of planar rigid panels into locally flexible panels with stiffness control. Comput Graph 2017;66:93–102.
[44] F. Bianconi, M. Filippucci, Digital wood design, Springer International Publishing Cham2019.
[45] Capone M, Lanzara E. Parametric kerf bending: manufacturing double curvature surfaces for wooden furniture design. Digital wood design: innovative techniques of representation in architectural design. 2019. p. 415–39.
[46] Gatóo A, Koronaki A, Chaudary A, Gin Y, Shah DU, Wiegand E, Hesselgren L, Ainoura M, Bakker R, Ramage M. Unfolding Timber-A future of design. Education and research in computer aided architectural design in Europe. 2022.
[47] ASTM D790. Standard test methods for flexural properties of unreinforced and reinforced plastics and electrical insulating materials. Am. Soc. Testing Mater. 1997.
[48] Zhang W, Neville R, Zhang D, Yuan J, Scarpa F, Lakes R. Bending of kerf chiral fractal lattice metamaterials. Compos Struct 2023;318:117068.
[49] Zhang Z, Jiang H, Bednarcyk BA, Chen Y. Greek key inspired fractal metamaterials with superior stretchability for tunable wave propagation. Adv. Mater. Technol. 2023;8(21):2300981.
[50] Travieso-Rodriguez JA, Jerez-Mesa R, Llumà J, Traver-Ramos O, Gomez-Gras G, Roa Rovira JJ. Mechanical properties of 3D-printing polylactic acid parts subjected to bending stress and fatigue testing. Materials 2019;12(23):3859.